F. Bottegoni, C. Zucchetti, G. Isella, M. Bollani, M. Finazzi, and F. Ciccacci, *Spin-charge interconversion in heterostructures based on group-IV semiconductors. Riv. Nuovo Cim.* **43**, 45–96 (2020).

DOI: 10.1007/s40766-020-0002-0

Spin-charge interconversion in heterostructures based on group-IV semiconductors

F. Bottegoni([1])(*), C. Zucchetti([1]), G. Isella([1]), M. Bollani([2]), M. Finazzi([1]) and F. Ciccacci([1])

([1]) *Dipartimento di Fisica, Politecnico di Milano, Piazza Leonardo da Vinci 32, 20133 Milano, Italy*

([2]) *Istituto di Fotonica e Nanotecnologie IFN-CNR, Piazza Leonardo da Vinci 32, 20133 Milano, Italy*

Summary. — Spin-charge interconversion phenomena are ubiquitous in solid-state physics and represent a powerful tool to investigate spin transport in metals, semiconductors and metal/semiconductor heterostructures. The possibility to convert a spin current into a charge current (and vice versa) allows for the design of efficient spin injection/detection schemes, even without the use of ferromagnets, to unravel fundamental spin transport properties. The article reviews the recent advances in the investigation of the spin-charge interconversion phenomena in platforms based on group-IV semiconductors. Convenient experimental architectures to inject and detect spin currents in Ge and Si are discussed, as well as diffusion models for spin transport in these semiconductors.

1. – Introduction

Spintronics, or spin-electronics, is the branch of solid-state physics which studies spin generation, transport and manipulation in solid-state environments [1]. Since the discovery of the giant magnetoresistence (GMR) [2, 3], spin-based devices have attracted a growing interest thanks to their industrial applications. In particular, sensors based on the GMR or tunneling magnetoresistence (TMR) [4, 5, 6] have been implemented in data storage.

More recently, spintronic devices based on the spin transfer torque (STT) [7, 8] have been developed. At variance from GMR, where the control of the charge flow is performed by the magnetization of ferromagnets (FM), the STT relies on the torque, exerted by the flow of a spin current, acting on the magnetization of a FM [9, 10].

(*) e-mail: federico.bottegoni@polimi.it

Typical structures for STT are composed of two FM layers with different magnetization directions separated by a thin non-magnetic metal layer. If a charge current is applied, the first FM acts as a spin polarizer, generating a spin current which is then injected in the second FM layer, where the spin-torque is exerted [10]. However, alternative approaches for the generation of spin currents are possible and, in particular, the conversion of a charge current into a spin current by means of spin-orbit coupling [11, 12, 13] is one of the most exploited. The effects which allow for the transformation of a charge current into a spin current, or viceversa, are generically named *spin-charge interconversion* (SCI) phenomena. In this frame, the torque exerted on ferromagnets by spin currents generated via the SCI is named *spin-orbit torque* (SOT) [14, 15]. This alternative route holds the promise of requiring less charge current density compared to STT [16].

In this sense, SCI phenomena have attracted the attention of the scientific community also because they represent a viable tool to detect spin currents by measuring the converted charge current [17]. Indeed, the ability of detecting spins is mandatory for the development of spin-based devices, and this is possible through SCI without the exploitation of ferromagnets.

Although spin-based devices have already been engineered in ferromagnetic-based platforms, the exploitation of semiconductors in market spintronics is still in an embryonic phase. In fact, a long-range magnetic order is the ultimate ingredient for the observation of GMR or TMR, while ordinary semiconductors are non-magnetic, due to the absence of spin-resolved bands at the Fermi level. In this respect, dilute magnetic semiconductors, *i.e.* semiconductors doped with magnetic impurities [18, 19, 20], could represent a possible solution. However, their application is still limited due to the small solubility of magnetic ions [21] and Curie temperatures well below room temperature [22].

Nevertheless, well-established techniques to generate *out-of-equilibrium* spin populations in semiconductors are available, either electrically [23, 24], optically [25, 26, 27], or mechanically [28, 29]. Therefore, semiconductors appear as the natural host materials for a ready integration of spintronic and electronic devices. In this frame, great advantages in terms of speed of data processing and power consumption are expected: in fact, as opposite to a charge current, a pure spin current is not associated with any charge flux [30]. Therefore, by associating information to the spin degree of freedom of electrons, it could be possible in principle to drastically reduce both the power consumption generated by Joule heating and the capacitive effects which limits the speed of electronic devices.

Moreover, in semiconductors spin is preserved for longer time scales compared to metals [31, 32, 33], and interface effects can give rise to a large spin-orbit coupling, which can be eventually used for spin manipulation [34, 17]. These premises led to the theoretical proposal, dated 1990, of a spin-based field-effect transistor [35, 36]. However, up to now, the experimental implementations of this concept are still not satisfactory [3, 37], despite the ongoing efforts [38, 39] and the proposed different approaches for a spintronic transistor [40, 41].

In this context germanium appears as a convenient platform for the implementation of spintronic devices, since the spin-orbit coupling is small enough to result in long spin-diffusion lengths [32, 33] but large enough to allow for an efficient optical spin injection [27]. Ge can also be exploited as a substrate for the growth of high-quality thin single-crystal heavy metal films [34]. Moreover, the Ge direct gap is tuned at the most widely exploited telecommunication window [42], and the 4% of lattice mismatch between Ge and Si allows for the integration of the materials in SiGe heterostructures [43, 44], which

can also be exploited in strain engineered microstructures [45].

The present paper is organized as follows: in Section **2** we introduce the fundamental concepts about spin-charge interconversion phenomena; Section **3** is devoted to the optical spin injection; in Section **4** the most relevant spin relaxation mechanisms are reviewed whereas in Section **5** and **6** the employed experimental techniques for spin-charge and charge-spin conversion are presented, respectively. Finally Section **7** reports on the experimental results obtained about the spin-related properties in semiconductors, with particular emphasys on Ge and Ge-based junctions.

2. – Spin-charge interconversion phenomena

The term *spin-charge interconversion* (SCI) encompasses for all the phenomena which convert a spin current into a charge current, or viceversa. In solids, these effects are driven by spin-orbit interaction (SOI), which affects the material transport properties depending on the spin-polarization state of the carriers.

The possibility of generating a spin accumulation from a charge current was first revealed by Dyakonov and Perel [11, 12] and then by Hirsch [46] and Zhang [47]. The phenomenon was named *spin Hall effect* (SHE), in analogy with the well known Hall effect, and was experimentally demonstrated in III-V semiconductors at low temperature by Kato et al. in 2004 [48]. The spin-charge conversion, performed via SHE, usually takes place in the bulk of materials, therefore we can consider it as a three-dimensional (3D-SCI) phenomenon.

Conversely, a pure two-dimensional SCI mechanism (2D-SCI) was first theoretically predicted by Edelstein in 1990 [13] [hence named *Edelstein* effect (EE) or *Rashba-Edelstein effect* (REE)], and then experimentally demonstrated by Rojas-Sanchez et al. in 2013 [49]. Although the macroscopic behavior is similar to SHE, the presence of spin-polarized surface/interface states is mandatory for this spin-charge conversion mechanism.

2˙1. *3D spin-charge interconversion.* – When a charge current density $\mathbf{j}$ is flowing in a material with SOI, the SHE generates a pure spin current density $\mathbf{j}_\mathrm{s}$. The latter is perpendicular to both $\mathbf{j}$ and the direction of the spin polarization of the carriers $\mathbf{u}_\mathrm{s}$. The phenomenological relation describing SHE is [50]:

$$\mathbf{j}_\mathrm{s} = \gamma\, \mathbf{j} \times \mathbf{u}_\mathrm{s}, \tag{1}$$

being γ the *spin-Hall angle*, representing the efficiency of SCI. Frequently, the γ parameter is expressed as the ratio between a *spin-Hall conductivity* $\sigma_\mathrm{SH} = \gamma\, \sigma_\mathrm{c}$ and the electrical conductivity σ_c.

The time reversal of the SHE is the *inverse spin Hall effect* (ISHE). In this case, the flow of a spin current density generates a charge current density:

$$\mathbf{j} = \gamma\, \mathbf{j}_\mathrm{s} \times \mathbf{u}_\mathrm{s}. \tag{2}$$

It is worth mentioning that ISHE can be exploited to detect spin currents [51]: in materials where SOI, and hence the spin-Hall angle γ, is large, ISHE can efficiently convert the spin current into a detectable charge current. When not dealing with materials where γ is large enough for an efficient detection, it is possible to transfer the spin population to

a second material with a relevant SOI, where efficient SCI might occur. In this case, this high-SOI material acts as a *spin detector*.

Microscopically, three different mechanisms can give rise to SCI. The first one is named *skew scattering* [50] and is associated with scattering centers, represented for instance by doping impurities. In this case, the propagation direction of a carrier after the scattering event is sensitive to its spin-polarization state, especially if the scattering center possesses a large atomic number and is therefore endowed by a large SOI. In atomic physics, when a high-energy incident electron beam is scattered by a high-Z nucleus, the same mechanism is known as *Mott scattering* [50].

The *side jump* mechanism is a lateral displacement of the carrier, depending on its spin state, during the scattering event [50]. Its origin is related to the local distortion of the incoming carrier wavefunction given by the impurity [52, 53, 54, 50]. Due to their link with collisions, *skew scattering* and *side jump* are defined as *extrinsic* mechanisms.

Spin-polarized carriers can also undergo *intrinsic* SCI. The latter originates from the geometrical phase, referred to as *Berry phase*, acquired by the wavefunction due to the introduction of relativistic effects in the bandstructure [55, 56], which become relevant in systems with large SOI [57].

2˙2. *2D spin-charge interconversion.* – (R)EE arises in the presence of spin-polarized surface or interface states. In particular, the removal of the spin degeneracy of the electronic states can originate from the structural inversion asymmetry (SIA), resulting in the *Bychkov-Rashba effect* [58], as shown in Fig. 1a. Spin-splitting can be also generated by the nontrivial topology of the system under investigation: this is the case of *topological insulators* [59] (TI), which show spin-split surface states with linear dispersion, crossing the Fermi level of the system (see Fig. 1c). Both in Rashba-split and topologically protected states, electron momentum and spin are locked in the reciprocal space and perpendicular to each other, as indicated in Fig. 1b-d. This is the key ingredient leading to SCI. Considering, for instance, the case of topological surface states and referring to Fig. 2, if an electric field $\mathbf{E} = E\mathbf{u}_{\mathrm{x}}$ is applied, a 2D charge current flows along the x-axis of the sample, which can be written in the frame of the Boltzmann transport equation as

$$\mathbf{j} = -\frac{q^2\,\tau_{\mathrm{m}}\,k_{\mathrm{F}}v_{\mathrm{F}}}{4\pi^2\,\hbar}\,\mathbf{E}, \tag{3}$$

where q is the elementary charge, τ_{m}, k_{F} and v_{F} are the momentum scattering time, the Fermi wave-vector and velocity, respectively. Within a semiclassical approach, the unbalance in the occupation of the electronic states, produced by the charge current density of Eq. 3, results in a spin unbalance, which can be related to a spin current density [60]:

$$\mathbf{j}_{\mathrm{s}} = -\frac{q^2\,k_{\mathrm{F}}}{4\pi^2\,\hbar}\,\mathbf{u}_{\mathrm{y}}. \tag{4}$$

Comparing eqs. (4) and (3) we can extract the parameter λ_{E} which, similarly to γ for SHE, evaluates the efficiency of the 2D-SCI:

$$\lambda_{\mathrm{E}} = \frac{j}{j_{\mathrm{s}}} = \tau_{\mathrm{m}}\,v_{\mathrm{F}}. \tag{5}$$

It is worth noticing that λ_E has the dimension of a length, hence the name *Edelstein length*. This is originated from the fact that j_s is a volume current density, while j is a surface current density, since it flows in the 2D states of the TI.

Conversely, if a spin current is injected in the TI states, by the definition of spin current, this means that spin-down electrons are injected into one of the two branches whereas opposite spins are extracted from the other one. Since it is possible to inject and extract spin-polarized carriers only in points of the reciprocal space with a well defined momentum, the injection of the spin current gives origin to a momentum unbalance, and consequently, a charge current. This is the principle of the *inverse Edelstein effect* (IEE).

The derivation for a Rashba gas is analogous [61]. Commonly, the 2D-SCI taking place in the surface states of a TI is named *Edelstein effect*, whereas the one concerning Rashba gases is called *Rashba-Edelstein effect*. In the latter case, the *Rashba-Edelstein length* is sligthly different [60]:

$$\lambda_{RE} = \frac{\alpha_R \tau_m}{\hbar}, \tag{6}$$

where the Rashba parameter α_R has been introduced.

It is worth noticing that in 2D electron gas, the spin-orbit interaction due to impurities may give origin to additional SCI terms, which cannot be easily disentangled from those related to the SIA due to the cooperative effects of the different spin-orbit mechanisms [62, 63].

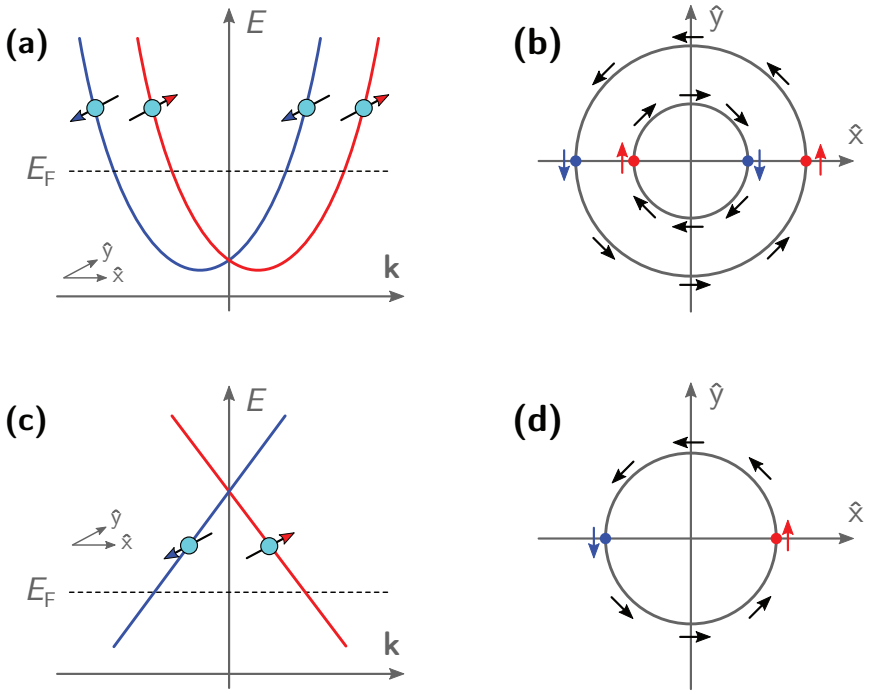

Figure 1.: Energy dispersion and Fermi contours resulting from Rashba effect (a,b) and of topological insulators (c,d).

3. – Optical Spin Injection

Much interest has been devoted in the past decades to dilute magnetic semiconductors, *i. e.* semiconductors doped with magnetic impurities [18, 19, 20], to induce a net spin polarization inside the material at equilibrium. However the small solubility of magnetic ions [21] and Curie temperatures below 200 K [22] still limit the applicability of this technology.

Conversely, to obtain a spin polarization in non-magnetic semiconductors it is necessary to bring the system out of equilibrium. This can be achieved by exploiting different techniques, relying on the transfer of angular momentum to the semiconductor. Different ways of injecting angular momentum have been explored in the literature: mechanically [28, 29], electrically [24] or optically [25, 26, 27]. Optical spin injection, also called *optical orientation*, is a powerful tool to obtain spin-polarized densities in the conduction band (CB) of semiconductors. First investigated by Lampel [25] in Si and later by Parsons [64], Safarov [65] and Meier [26] in III-V materials, optical orientation relies on the transfer of angular momentum from impinging photons to the photoexcited electrons.

3˙1. *Optical transitions at the* Γ *point.* – Optical orientation allows generating a population of spin-polarized photoelectrons in the CB of a semiconductor, when the semiconductor is illuminated with circularly-polarized (CP) light.

In Ge, the optical gap for direct transitions is at the Γ point of the Brilluoin zone (see Fig. 3a). The electronic states at Γ can be expressed as a linear combination of atomic orbitals through the Clebsch-Gordan coefficients [66], by exploiting the spherical harmonics $Y_l^{m_l}$. The results are reported in Tab. I. Although spherical harmonics describe only the angular part of the wavefunction, modifications induced by SOI on the radial part can be usually neglected. As a consequence, we can consider the same radial dependence for heavy holes (HH), light holes (LH), and split-off (SO) states in the valence band (VB) [27].

To investigate the optical orientation process, we calculate the rate of transitions from the initial state $|\varphi_\mathrm{i}\rangle$ to the final state $|\varphi_\mathrm{f}\rangle$ due to an external perturbation by means of

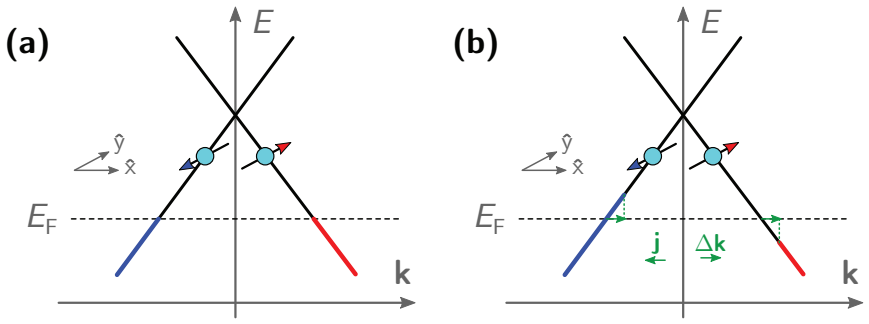

Figure 2.: Sketch of the occupation of the spin-split linear branches (a) at the thermodynamic equilibrium and (b) when a charge current is applied. In this case, the $\Delta\mathbf{k}$ wave-vector shift unbalances the spin-up and -down populations: Edelstein effect. Conversely, if a spin current is injected, spin-up states are filled and spin-down are emptied, thus resulting in a momentum unbalance, which means a charge current: inverse Edelstein effect.

Band	$j\,\lvert j, m_j\rangle$	**Spherical harmonics expansion**
CB	$\lvert 1/2, 1/2\rangle$	$Y_0^0\,\lvert\uparrow\rangle$
	$\lvert 1/2, -1/2\rangle$	$Y_0^0\,\lvert\downarrow\rangle$
LH	$\lvert 3/2, 1/2\rangle$	$i\sqrt{1/3}\,Y_1^1\,\lvert\downarrow\rangle + i\sqrt{2/3}\,Y_1^0\,\lvert\uparrow\rangle$
	$\lvert 3/2, -1/2\rangle$	$i\sqrt{1/3}\,Y_1^{-1}\,\lvert\uparrow\rangle + i\sqrt{2/3}\,Y_1^0\,\lvert\downarrow\rangle$
HH	$\lvert 3/2, 3/2\rangle$	$-iY_1^1\,\lvert\uparrow\rangle$
	$\lvert 3/2, -3/2\rangle$	$-iY_1^{-1}\,\lvert\uparrow\rangle$
SO	$\lvert 1/2, 1/2\rangle$	$i\sqrt{1/3}\,Y_1^0\,\lvert\downarrow\rangle - i\sqrt{2/3}\,Y_1^{-1}\,\lvert\uparrow\rangle$
	$\lvert 1/2, -1/2\rangle$	$-i\sqrt{1/3}\,Y_1^0\,\lvert\uparrow\rangle + i\sqrt{2/3}\,Y_1^1\,\lvert\downarrow\rangle$

TABLE I.: Total angular momentum quantum numbers and spherical harmonics expansion of the wavefunctions for states close to the Γ point [26].

the Fermi golden rule. When the perturbation is a monochromatic wave at a frequency ω with amplitude E_0, within the electric dipole approximation the Fermi golden rule gives the following expression for the transition rate $W_{\rm if}$ between the initial and final state [67]:

$$W_{\rm if} = \frac{2\pi}{\hbar}\left(\frac{qE_0}{m_0\omega}\right)^2 M_{\rm if}(\mathbf{k})^2\,\delta(E_{\rm i} - E_{\rm f} + \hbar\omega), \tag{7}$$

being $M_{\rm if}(\mathbf{k}) = |\mathbf{e}\cdot\langle\varphi_{\rm f}|\hat{\mathbf{p}}|\varphi_{\rm i}\rangle|$, with $\hat{\mathbf{p}} = -i\hbar\nabla$ the momentum operator, $\mathbf{e}$ unit vector of the polarization of the electric field, and the Dirac delta ensuring energy conservation, with $E_{\rm f}$ and $E_{\rm i}$ being the energy of the initial and the final state, respectively. Left- (right-) handed CP light $\sigma^{+(-)}$ carries angular momentum ±1, in units of $\hbar$, directed along the direction of the propagation [68]. In this case, angular momentum conservation implies that only the optical transitions with $\Delta m_l = \pm1$ are allowed. The direct optical transitions for $\sigma^{+(-)}$-polarized light are obtained from Tab. I and are reported in Fig. 3b. Thus, σ^- light (blue arrows in Fig. 3b) promotes only electrons to spin-up states in CB from the HH band, and to spin-down states from LH and SO bands. The opposite stands for σ^+ polarization (red arrows in Fig. 3). The principle of optical orientation lies on the fact that transitions from HH to CB have an intensity three times larger than transitions from LH to CB, whereas transitions from SO to CB have an intensity twice as large as transitions from LH to CB, as schematically shown in Fig. 3 [26]. In this case, when the photon energy is tuned at the direct gap ($\hbar\omega = E_{\rm dg}$), only HH and LH states are involved in optical transitions and a photogenerated carrier spin-polarization at the generation time $P_{\rm n,0} = 50\%$ can be reached in the CB of Ge, with unit vector $\mathbf{u}_{\rm s}$ parallel to the direction of the wavevector of the light in the semiconductor. When the photon energy is $\hbar\omega = E_{\rm dg} + \Delta_0$, the transitions from the SO band become allowed and the spin-polarization decreases to 0%.

In bulk III-V semiconductors, such as GaAs ($E_{\rm g} = 1.42$ eV at room temperature), the electronic states at the Γ point of the Brillouin zone can be still expressed with the same linear combinations of spherical harmonics, presented in Tab. I. Therefore, the optical orientation process is analogous to the one discussed for bulk Ge.

3˙2. *Out of* Γ *transitions.* – When the photon energy is larger than $E_{\rm dg}$ all the possible transitions within the Brillouin zone have to be accounted. This implies the integration

of the Fermi golden rule [eq. (7)] over the whole reciprocal space. Neglecting constants:

$$W_{\mathrm{if}} \propto \int M_{\mathrm{if}}(\mathbf{k})^2 \delta(E_{\mathrm{i}} - E_{\mathrm{f}} + \hbar\omega)\, d^3\mathbf{k}. \tag{8}$$

A rigorous calculation of the electron spin polarization as a function of the incident photon energy in bulk Ge has been performed by Rioux and Sipe within a 8×8 $\mathbf{k} \cdot \mathbf{p}$ model [69]. The calculated spectrum of $P_{\mathrm{n},0}$ is shown in Fig. 4 (orange line).

It is also possible to employ a rougher model in which $M_{\mathrm{if}}(\mathbf{k}) \approx M_{\mathrm{if}}(0)$. Within this picture, the relative weights of the matrix elements from HH, LH and SO transitions out of Γ equal the ones calculated in the previous section at the Γ point:

$$W_{\mathrm{if}} \propto M_{\mathrm{if}}(0)^2 \int \delta(E_{\mathrm{i}} - E_{\mathrm{f}} + \hbar\omega)\, d^3\mathbf{k} = M_{\mathrm{if}}(0)^2\, \varrho_{\mathrm{if}}. \tag{9}$$

ϱ_{if} is the *joint density of states* (JDOS) and within the effective mass approximation can be expressed analytically as [70]:

$$\varrho_{\mathrm{if}} = \frac{1}{2\pi^2}\left(\frac{2m_{\mathrm{r}}^*}{\hbar^2}\right)^{3/2} \sqrt{\hbar\omega - E_{\mathrm{g}}}, \tag{10}$$

being m_{r}^* the reduced effective mass of the VB and CB states involved in the transition, and $E_{\mathrm{g}} = E_{\mathrm{dg}}$ for (HH, LH) $\rightarrow$ CB and $E_{\mathrm{g}} = E_{\mathrm{dg}} + \Delta_0$ for SO $\rightarrow$ CB transitions. The resulting $P_{\mathrm{n},0}(\hbar\omega)$ is reported in Fig. 4 (blue line).

Optical spin injection can also be performed by means of indirect transitions: in fact, it has been recently demonstrated both theoretically [71] and experimentally [72] that phonon-mediated optical transitions can induce a net spin density at the Si indirect gap, with a maximum spin polarization $P \approx 5\%$ if the incident photon energy is tuned to the Si indirect gap ($E_{\mathrm{ig}} = 1.1$ eV at room temperature).

Finally, note that we have so fare considered only the spin population generated by the photoexcited electrons in the CB. In the optical orientation process, also holes are

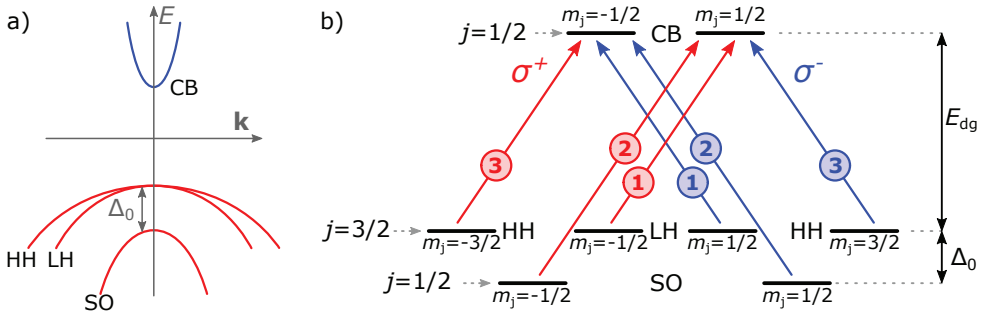

Figure 3.: a) Sketch of the Ge bandstructure around the Γ point of the Brillouin zone, where the conduction band (CB), heavy-hole (HH), light-hole (LH) and split-off (SO) states are highlighted. b) Optical transitions allowed with left- (right-) handed CP light $\sigma^{+(-)}$ at the Γ point of Ge Brillouin zone. The numbers in the circles show the relative intensity of the transitions.

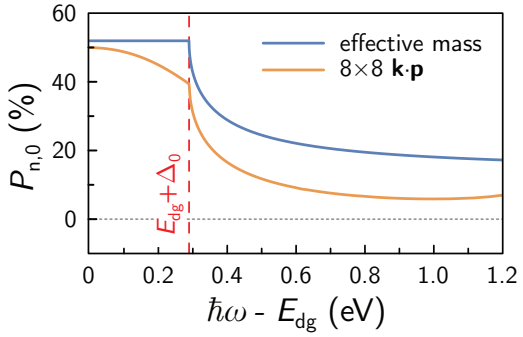

Figure 4.: Polarization spectra of photogenerated electrons at the generation time, calculated with effective mass approximation, from Ref. [73] (blue line), and 8×8 $\mathbf{k} \cdot \mathbf{p}$ calculations, from Ref. [69] (orange line).

photoexcited in the VB with a net spin polarization [69]. However, we will see in Sec. **4**˙4 that holes do not actively contribute to spin transport, at least in unbiased samples.

4. – Spin lifetime in semiconductors

4˙1. *Elliot-Yafet spin relaxation mechanism.* – The Elliott-Yafet mechanism is the most effective spin relaxation channel occurring in semiconductors with inversion symmetry, like Ge [74, 75] and it is related to the effective magnetic field acting on a particle during a scattering event that involves impurity centers (for instance related to the semiconductor doping) or, similarly, an electron-phonon scattering due to the lattice potential perturbation [50]. A detailed presentation of the mechanism can be found in Ref. [76]. In particular, in multivalley semiconductors such as Ge, spin-polarized electrons diffusing at the bottom of the conduction band are scattered between the CB equivalent minima by phonons, strongly limiting electron spin lifetime to few nanoseconds [31, 77].

Here we exploit the approximation of Guite and Venkataraman [78], in which momentum τ_{m} and spin lifetime τ_{s} are proportional to each other, and the proportionality constant is given by key parameters of the bandstructure:

$$\left(\tau_{\mathrm{s}}^{\mathrm{EY}}\right)^{-1} = \left(\frac{\Delta_0}{E_{\mathrm{dg}}+\Delta_0}\,\frac{E_{\mathrm{k}}}{E_{\mathrm{dg}}}\right)^2 {\tau_{\mathrm{m}}}^{-1}, \tag{11}$$

where E_{k} is the electron kinetic energy. As an example, in Fig. 5 (a) we plot the calculated spin lifetime due to the Elliott-Yafet relaxation mechanism in Ge at room temperature and the partial contributions related to scattering with impurities ($\tau_{\mathrm{s,imp}}^{\mathrm{EY}}$) and phonons ($\tau_{\mathrm{s,ph}}^{\mathrm{EY}}$) as a function of the doping concentration N_{d}. Scattering with phonons (impurities) is the leading process dominating spin relaxation in low- (highly-) doped Ge. In Fig. 5 (b), the dependence of $\tau_{\mathrm{s}}^{\mathrm{EY}}$ on the electron kinetic energy E_{k} is reported for $N_{\mathrm{d}} = 5 \times 10^{17}$ cm^{-3}. It is worth mentioning that the value of $\tau_{\mathrm{s,ph}}^{\mathrm{EY}}$ that we estimate for thermalized electrons nicely agrees with the predictions of the more refined $\mathbf{k} \cdot \mathbf{p}$ model employed in Refs. [31, 77] ($\tau_{\mathrm{s,ph}}^{\mathrm{EY}} \approx 5$ ns).

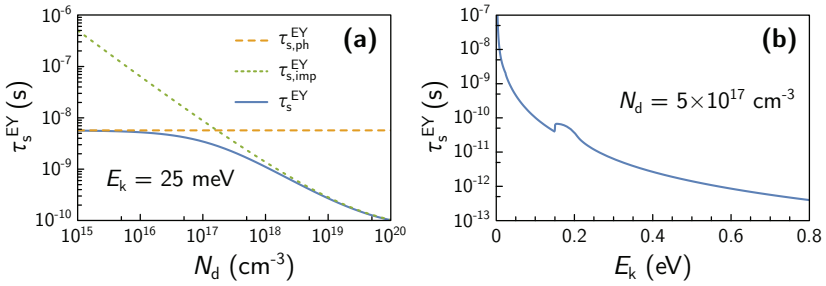

Figure 5.: Spin relaxation time as a function of (a) the doping concentration at $E_k = 25$ meV, and (b) kinetic energy for $N_a = 5 \times 10^{17}$ cm^{-3}. In panel (a) we report the Elliott-Yafet spin depolarization due to scattering with phonons (orange dashed line), impurities (green dotted line) and their sum (blue continuous line).

4˙2. *Bir-Aronov-Pikus spin relaxation mechanism.* – The Bir-Aronov-Pikus (BAP) spin relaxation channel is active in case of electron-hole scattering [79]. In this case, the exchange interaction can transfer the polarization of the electron to the hole, where the spin quickly depolarizes, as detailed in the next section. Thus, the BAP mechanism occurs when an equilibrium holes population is present, i.e., in p-doped semiconductors [76, 50]. The related spin relaxation time is [76, 80]:

$$\left(\tau_s^{\mathrm{BAP}}\right)^{-1} = \frac{2}{\tau_{s0}^{\mathrm{BAP}}} \frac{v_{\mathrm{F},h}}{v_{\mathrm{B}}} \frac{E_k}{E_{\mathrm{F},h}} N_a {a_{\mathrm{B}}}^3, \tag{12}$$

being $v_{\mathrm{F},h}$ and $E_{\mathrm{F},h}$ the Fermi velocity and energy for holes, respectively, N_a the number of acceptors, v_{B} and a_{B} the Bohr velocity and radius, respectively. τ_{BAP}^{s0} is given by the following expression [80]:

$$\left(\tau_{s0}^{\mathrm{BAP}}\right)^{-1} = \frac{3\,\pi}{64\,\hbar} \frac{{\Delta E_{\mathrm{SR}}}^2}{E_{\mathrm{B}}}, \tag{13}$$

where ΔE_{SR} is the short-range exchange splitting of the exciton ground state and E_{B} the exciton Bohr energy. In the case of Ge, we estimate $a_{\mathrm{B}} \approx 6.4$ nm, $\Delta E_{\mathrm{SR}} \approx 58$ μeV [81], $E_{\mathrm{B}} \approx 6.9$ meV. Despite BAP scattering is the leading term for a thermalized electron population in p-doped Ge, it rapidly becomes negligible compared to the other scattering processes as the electron energy is increased even slightly, as one can appreciate by comparing Fig. 6, in which we plot some indicative spin relaxation time for this mechanism, and Fig. 5.

4˙3. *Dyakonov-Perel spin relaxation mechanism.* – In semiconductors without inversion symmetry, the spin degeneracy of the electronic states in CB is removed out of the Γ point of the Brillouin zone due to SOI [82, 83]. This can be interpreted as the effect of an effective magnetic field $\mathbf{B}(\mathbf{p})$, depending on the electron momentum $\mathbf{p}$, which provides for the additional term in the Hamiltonian of the system [82]

$$H_{\mathrm{DP}} = \hbar \mathbf{B}(\mathbf{p}) \cdot \mathbf{S}, \tag{14}$$

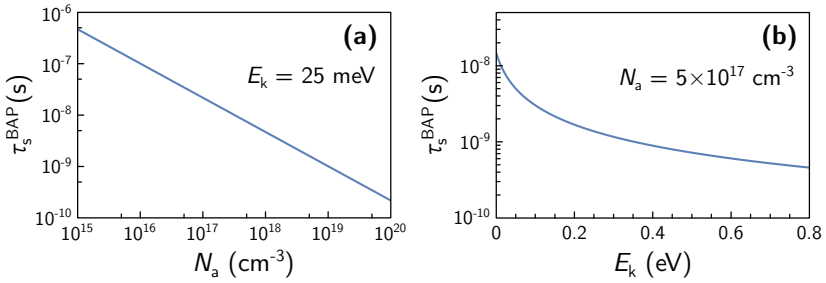

Figure 6.: BAP relaxation time as a function of (a) the doping concentration at $E_k = 25$ meV, and (b) kinetic energy for $N_a = 5 \times 10^{17}$ cm^{-3}.

where $\mathbf{S}$ represents the electron spin. Since $\mathbf{B}(\mathbf{p})$ has different orientation as a function of time, due to the fact that the electron momentum $\mathbf{p}$ changes in time because of momentum scattering, the rotation of the electron spin around the effective magnetic field causes the spin relaxation. It can be demonstrated that $\tau_s^{-1} \propto \tau_m$, where τ_s and τ_p are the electron spin and momentum relaxation time, respectively [82].

4˙4. *Hole relaxation.* – A good description for the holes in the valence band is given by the Luttinger Hamiltonian [84, 85]:

$$\mathscr{H}_L = \frac{\hbar^2}{2m_0}\left[(\gamma_1 + {}^5\!/_2\,\gamma_2)k^2 - \gamma_2(\mathbf{k}\cdot\mathbf{J})^2\right], \tag{15}$$

being $\gamma_{1,2}$ the Luttinger parameters and $\mathbf{J} = (\mathbf{J}_x, \mathbf{J}_y, \mathbf{J}_z)$ the matrices of the total angular momentum. In the valence band, the effective magnetic field generated by SOI is much larger than the one in the conduction band: therefore the Dyakonov-Perel spin relaxation mechanism for holes is more efficient, leading to hole spin lifetime of the order of ≈ 100 fs, comparable to the momentum relaxation time. This is the reason why the contribution from holes in the spin transport can be neglected.

Experimentally, Hilton and Tang have determined a value of ≈ 110 fs for the spin relaxation of HH in GaAs [86]. Conversely, for GaAs a spin lifetime of ≈ 0.1 ns is expected for thermalized electrons at room temperature [87]. Also in Ge, hole spin lifetimes of the order of hundreds of fs have been reported in the literature [88], whereas the electron spin lifetime can reach ≈ 10 ns in low-doped Ge samples [32].

4˙5. *Spin relaxation of 2D electrons.* – In 2D systems, as a consequence of the Rashba effect, SIA generates an effective magnetic field, coupled to the spin magnetic dipole $\boldsymbol{\mu}_s$ and expressed as

$$\mathbf{B}_R = \frac{\alpha_R}{g_s\mu_B}(\mathbf{k}\times\hat{\mathbf{z}}). \tag{16}$$

In this respect, it is worth mentioning that Rashba effective magnetic fields have been observed in the literature by Meier et al. [89] in GaAs/InGaAs quantum wells.

5. – Experimental techniques: spin-to-charge conversion

In spin-to-charge conversion measurements the electric signal generated by the conversion of a spin current, via the ISHE or the I(R)EE, is detected. The spin current can be injected electrically, i.e. by exploiting the *spin pumping* [90], or optically: in this paper, we will focus our attention on optical spin injection (see Sec. **3**). This procedure was first employed by Ando et al. [91, 92] in 2010 in a Pt/GaAs junction. In what follows, we first consider the experimental technique allowing for the generation of a detectable population of spin-polarized electrons in semiconductors and then we explicitly study the transport of spins in the illustrative case of an heavy metal (HM)/Ge junction.

5˙1. *Optical generation of spins.* – The typical experimental apparatus for photoinduced spin-charge conversion measurements is sketched in Fig. 7 (a). The light source consists of a supercontinuum laser, which emits a 4.5 W-intense collimated light beam, in a broad wavelength range, between 400 nm and 2 µm. Alternatively, fiber-pigtailed continuous wave laser diodes are employed. The monochromatized light beam passes through a polarizer and a *photoelastic modulator* (PEM), which modulates the circular polarization of the light at 50 kHz. The light is then focused on the sample by a lens or an objective and the detected electric signal is demodulated by a lock-in amplifier at the PEM frequency.

Hereafter, we consider an HM continuous film grown on the top of a semiconductor substrate, in particular Ge, as shown in Fig. 7 (b). In this case an high-SOI material is in direct contact with the semiconductor, which is exploited as a spin generator by means of the optical orientation technique, while the HM works as a spin detector. In order to detect the charge current in the HM, generated by the SCI, two ohmic contacts (typically Au/Ti) are deposited on the top of the HM layer, as shown in Fig. 7 (b). Based on the reference frame of Fig. 7 (b), we can make some general consideration about the geometry of the experiment: the ohmic contacts are sensitive only to a charge current density directed along the y axis. The spin population is injected into the semiconductor and then transferred to the HM, thus the spin current flows along the z axis. Based on the phenomenological ISHE relation [eq. (2), the same holds for I(R)EE], only electrons

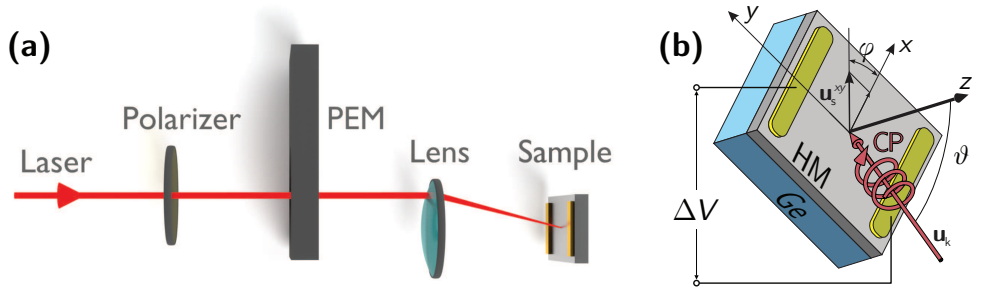

Figure 7.: Apparatus for optically-induced spin-to-charge conversion. (a) A laser beam passes through a polarizer and a PEM. The polarization of the exit beam is modulated at 50 kHz between left and right CP. A lens (or an objective) focuses the light on the sample. Since the beam partially fills off-axis the lens, the light is focused on the sample at grazing incidence. (b) φ and ϑ are the azimuthal and polar angles of the incident light, respectively.

with a spin polarization along the x axis can be detected [91, 92, 93, 72]. Thus, the injection of an in-plane spin component is mandatory to detect a spin-related charge current in the HM film.

The spin polarization of the photoexcited electrons $\mathbf{P}_{\mathrm{n},0}$ is parallel to the direction of the light wavevector $\mathbf{u}_{\mathrm{k}}$ inside Ge (see Sec. **3**). Thus, to obtain an in-plane projection of the spin $P^x_{\mathrm{n},0}$, it is convenient to illuminate the semiconductor at grazing incidence. This is possible if the laser beam partially fills off-axis the lens, or the objective [Fig. 7 (a)]. Notably, the selectivity to $P^x_{\mathrm{n},0}$-polarized electrons generates an angular (ϑ and φ) dependence of the spin-charge conversion signal which is a viable tool to confirm the spin-related nature of the detected electric signal, as explained in the second paragraph of Sec. **5**˙2.

Unfortunately, the illumination of the sample at grazing incidence degrades the spatial resolution of the exprimental setup. From the Rayleigh criterion [94], one can define the spatial resolution of the optical system Δr as:

$$\Delta r \sim \frac{f\lambda}{a} \tag{17}$$

being f the lens (or objective) focal length, λ the photon wavelength and a the beam aperture. To illuminate the sample at grazing incidence, the aperture diameter of the lens is partially filled (out of axis), thus reducing a. Despite the strong dependence on λ and on the characteristic parameters of the objectives, typical sizes of the spotsize of the focused beam are not smaller than some micrometer. Moreover, strong aberrations are present in the case of high values of ϑ.

A viable route to overcome the above issue consists in a metal pattern on the top of the semiconductor: it can be demonstrated that, under the edges of the metal, a sizable in-plane component of the spin is generated, even at normal incidence. This possibility has been first shown by Bottegoni et al. [95] in 2014. This happens both if the pattern is realized on the top of a flat metal layer grown on a semiconducro [95], or directly on the top of the semiconductor substrate [32]. Referring to the particular case of a metal pattern on a Ge substrate [see Fig. 8 (a)], when the CP laser beam impinges on one edge of the metallic pad, the component of the field which is perpendicular to the edge (E_x) induces an electric dipole in the metal, generating a near field in the semiconductor with a component directed along z [Fig. 8 (a)]. The latter is coupled to the E_y component of the propagating CP wave. Since E_z and E_y have a phase shift of $\pi/2$, an elliptically-polarized electric field is produced in the yz plane. Upon absorption of this field in the semiconductor, a spin-oriented electron population is generated in the CB of the Ge with a spin polarization along the x axis. Moreover, the direction of E_z is opposite at opposite edges of the pad, thus the spin populations at correspondence with opposite edges of the metal stripe are polarized in opposite directions.

This pictorial model has been rationalized with finite-difference time-domain (FDTD) numerical simulations in Ref. [95]. In Fig. 8 (b), we report the results of the calculations for a Pt stripe patterned on the top of a Pt/Ge system. The figure shows the Stokes parameter $c_x = 2\,\mathfrak{Im}(E_z\,E_y{}^*)$, which accounts for the light ellipticity in the direction perpendicular to the x axis [96], i.e., generating electrons with a polarization directed along x. Opposite spin polarizations are obtained at the opposite edges of the Pt pad. Notably, at variance with the grazing-incidence case, the spin population is strongly localized (at the time of the generation) within a small region below the Pt edges. The results of Fig. 8 (b) accounts for the incidence of a CP plane wave, but a similar situation occurs in the case of a focused laser beam [95].

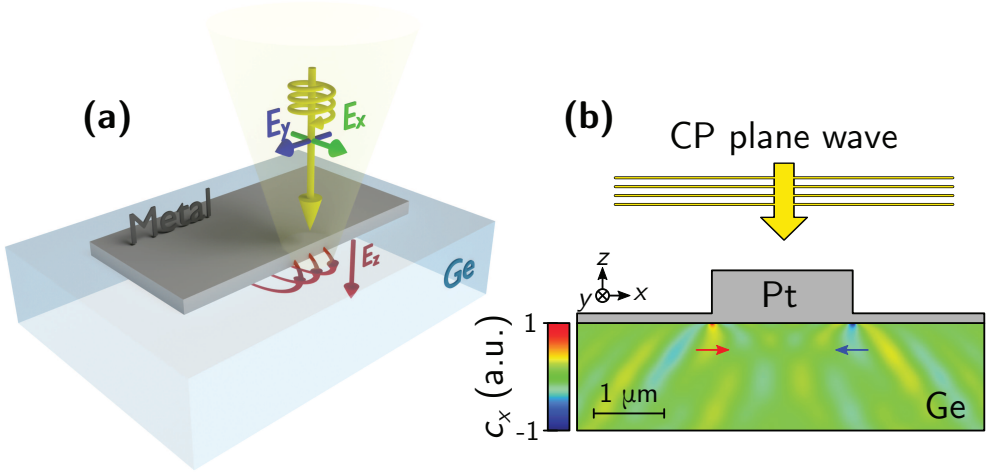

Figure 8.: Principles of normal incidence generation of in-plane spin. (a) The metal pattern provides for the spatial modulation of the amplitude and phase of the electromagnetic wave, which results in an elliptically-polarized electric field below the its edges. This generates spin-polarized electrons along the x axis. (b) FDTD calculation of the c_x Stokes parameter, proportional to the spin polarization along x, in a thin Pt patterned metal film onto a Ge surface.

5˙2. *Spin generation and transport in HM/semiconductor junctions.* – In this paragraph, we describe the influence of the HM layer on the optical properties of the light illuminating the sample. We determine the spatial distribution of photogenerated spin-polarized carriers in the semiconductor, and the resulting spin current density injected into the HM.

5˙2.1. *Optical analysis.* The presence of the HM affects both the light intensity and CP. Performing an optical analysis on a thin metal film, deposited onto a semiconductor substrate, it is possible to express the electric signal at the ohmic contacts as [91, 92]:

$$\Delta V \propto t_s t_p \, I_{air} \, \mathrm{DCP}_{air} \, \cos(\vartheta_{SC}) \, \mathrm{tg}(\vartheta) \cos(\varphi), \tag{18}$$

where $t_{s(p)}$ represent the light transmission coefficients, I_{air} and DCP_{air} are the intensity and DCP of the incoming light beam in air, whereas ϑ_{SC} and ϑ are the polar angles in the semiconductor and in air, respectively, and φ is the azimuthal angle. The angular dependence on ϑ and φ [defined in Fig. 7 (b)] are reported in Fig. 9 for a Pt(4 nm)/Ge junction, although, for an incident photon energy $\hbar\omega = 0.8$ eV, the trend is rather universal [91]. We notice that the maximum of the signal is observed for $\vartheta \approx 65°$, and that, for small ϑ angles, $\Delta V \propto \vartheta$.

5˙2.2. *Spatial distribution of the injected spin population.* The information about the distribution of the spins inside the semiconductor substrate allow for quantitative analysis of the spin transport. To estimate the spin current density $j_{s,0} = j_s(z = 0)$ injected into the HM from the semiconductor, we need to solve the coupled drift-diffusion and

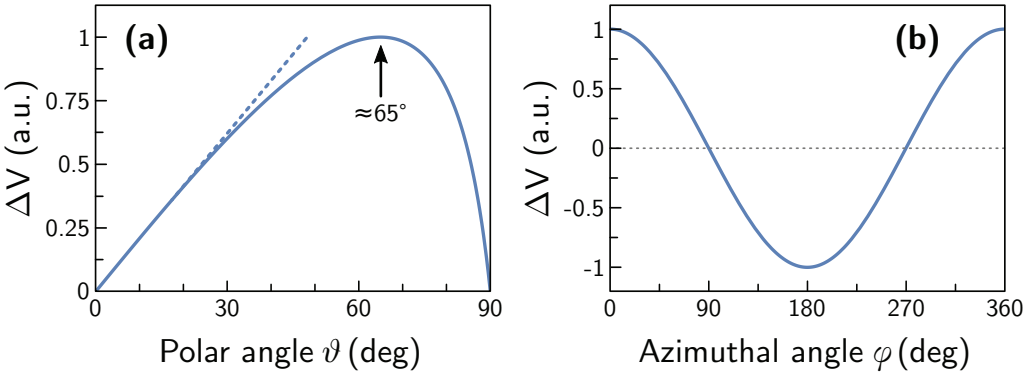

Figure 9.: Angular dependence of the spin-to-charge conversion signal measured at the Ohmic contacts ΔV on the polar angle ϑ (a), and the azimuthal angle φ (b). The dotted line in (a) shows a linear fit for small ϑ angles.

continuity equations for charge and spin, respectively, where generation and recombination terms are present. In general, the solution cannot be expressed analytically. Thus, to simplify the problem we neglect the contribution given by the gradient of the in-plane xy carrier concentration, and focus only on the one dimensional problem along the z axis [see Fig. 7 (b) for the reference system]. In the geometry of Fig. 10, we consider the semiconductor as a semi-infinite medium extending for $z < 0$, with the HM/semiconductor interface at $z = 0$. The light illuminates the system from the HM side, propagating towards negative values of z. Therefore, steady-state spin drift-diffusion equations for the spin population in the semiconductor are written as [97, 98]:

$$\frac{1}{q}\frac{\partial j_{\mathrm{s}}}{\partial z} = \frac{s}{\tau_{\mathrm{s}}} + w_{\mathrm{n}} s p - P_{\mathrm{n},0}\Phi_{\mathrm{ph}}\alpha e^{\alpha z}, \tag{19a}$$

$$j_{\mathrm{s}} = q\left(\mu s E + D\frac{\partial s}{\partial z}\right), \tag{19b}$$

being w_{n} the electron-hole recombination rate, Φ_{ph} the flux of photons transmitted to the semiconductor, α the absorption coefficient, and p the concentration of holes. Since

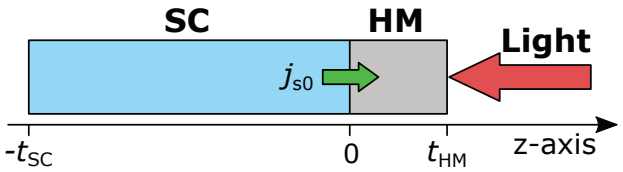

Figure 10.: A HM layer of thickness t_{HM} lies on the top of a semiconductor (SC) substrate of thickness t_{SC}. In a semi-infinite approximation, $t_{\mathrm{SC}} \to \infty$. The light illuminates the junction from the side of the HM layer, and we define $j_{\mathrm{s},0}$ as the spin current density injected into the HM from the semiconductor.

typical electron-hole recombination times in semiconductors lie in the 10 µs − 3 ms range [99], this term does not affect spin profile, thus we disregard its contribution. Moreover, as a first coarse approximation, we also neglect the electric field E generated by the charge transfer across the Schottky junction. We thus obtain the following simplified spin-diffusion equation with a generation term:

$$\frac{\partial^2 s}{\partial z^2} - \frac{s}{{\ell_\mathrm{s}}^2} = -\frac{P_{\mathrm{n},0}\Phi_\mathrm{ph}\alpha}{D}\, e^{\alpha z}, \tag{20}$$

where we have exploited the relation between the spin lifetime τ_s and the spin diffusion length $\ell_\mathrm{s} = \sqrt{D\tau_\mathrm{s}}$.

The general solution is:

$$s(z) = \tau_\mathrm{s}\, P_{\mathrm{n},0}\Phi_\mathrm{ph}\alpha\, e^{\alpha z} + c_1\, e^{z/\ell_\mathrm{s}} + c_2\, e^{-z/\ell_\mathrm{s}}, \tag{21}$$

being $c_{1,2}$ constants to be determined by the boundary conditions. We impose that the spin density vanishes in the bulk of the semiconductor, i.e., for $z \to -\infty$ leading to $c_2 = 0$. Moreover, since the value of the spin diffusion length in the HM is usually a few nanometer only, therefore negligible with respect to the typical values of the spin diffusion length in semiconductors, we can set $s(z = 0) = 0$ [97]. With these conditions we get:

$$s(z) = \frac{P_{\mathrm{n},0}\Phi_\mathrm{ph}}{D}\, \frac{\alpha {\ell_\mathrm{s}}^2 \left(e^{\alpha z} - e^{-z/ls}\right)}{1 - \alpha^2 {\ell_\mathrm{s}}^2}, \tag{22a}$$

$$j_\mathrm{s}(z) = qP_{\mathrm{n},0}\Phi_\mathrm{ph}\, \frac{\alpha\ell_\mathrm{s}\left(\alpha\ell_\mathrm{s}\, e^{\alpha z} - e^{-z/ls}\right)}{1 - \alpha^2 {\ell_\mathrm{s}}^2}. \tag{22b}$$

From the expressions above, we can extract the value of the spin current injected into the HM. By evaluating the spin current density at $z = 0$, we get [100]:

$$j_{\mathrm{s},0} = -qP_{\mathrm{n},0}\Phi_\mathrm{ph}\, \frac{\alpha\ell_\mathrm{s}}{1 + \alpha\ell_\mathrm{s}} = -\xi \frac{P_{\mathrm{n},0}\alpha\ell_\mathrm{s}}{1 + \alpha\ell_\mathrm{s}}, \tag{23}$$

where $\xi = q\Phi_\mathrm{ph}$ is a constant. Assuming $P_{\mathrm{n},0} > 0$ we get $j_{\mathrm{s},0} < 0$. The expression of eq. 23 is analogous to the one developed by Spicer [101, 102] and Pierce et al. [103] concerning photoemission (in case spin-polarized) and photoconductivity measurements in bulk semiconductors. For this reason, in the following, we call this approach the *Spicer-like model*. The limits of applicability of the Spicer-like model will be discussed in the last paragraph of this section.

5˙2.3. *Spin-to-charge conversion in the heavy-metal layer*. It is interesting to correlate the spin current density injected into the HM layer to the potential difference generated at the Ohmic contacts [see Fig. 7 (b)]. Inside the spin detector, since no generation term or electric field is present, we just solve the spin drift-diffusion equation along the z-axis, which reads:

$$\frac{\partial^2 s}{\partial z^2} = \frac{s}{{\ell_\mathrm{s}}^2}. \tag{24}$$

We assume that the spin current density at $z = 0$, i.e., at the HM/semiconductor interface, is $j_{s,0}$, as calculated in eq. (23). Conversely, at $z = t_{HM}$, being t_{HM} the thickness of the HM layer, we set $j_s = 0$, imposing that the spin current cannot leak from the HM surface. With these boundary conditions, the spin current density inside the HM is:

$$j_s(z) = j_{s,0}\,\mathrm{csch}\left(\frac{t_{HM}}{\ell_s^{HM}}\right)\sinh\left(\frac{t_{HM}-x}{\ell_s^{HM}}\right), \tag{25}$$

being ℓ_s^{HM}, the spin-diffusion length in HM. We define $j_s^{av} = \langle j_s(z)\rangle_z$ as the spin current density averaged over the thickness t_{HM} of the HM layer [92]. We obtain:

$$j_s^{av} = j_{s,0}\,\frac{t_{HM}}{\ell_s^{HM}}\tanh\left(\frac{t_{HM}}{2\ell_s^{HM}}\right), \tag{26}$$

which is the expression used in Refs. [92, 104]. Therefore, the potential difference at the extrema of the illuminated region is $\Delta V_{ISHE} = \rho\, a\, j_s^{av}$, being ρ the electrical resistivity and a the spot diameter of the focused laser beam. Consequently, the measured potential difference ΔV at the Ohmic contacts under open circuit conditions is $\Delta V = \Delta V_{ISHE}\,\pi a/(4d_x)$, being d_x the dimension of the HM film along the x axis [104].

5˙2.4. *Validity of the Spicer-like model*. The Spicer-like model introduces a simple analytical formula to quantify the spin current density injected into the HM film. It is important to compare the results of eq. (23) with the outcome of a finite element method (FEM) analysis, where the spin-drift diffusion equation is numerically solved both in the semiconductor and the HM. The geometry of the problem (Fig. 10) and the basic equations to be solved [eqs. (19)] are the same. Moreover, at variance with the Spicer-like model, we can explicitly consider the built-in electric field of the Schottky junction [105]. We apply the boundary conditions: $s(z = -t_{SC}) = 0$ and $j_s(z = t_{HM}) = 0$. The former equation accounts for the impossibility to have a net spin density at the bottom Ge surface, provided that t_{SC} is much larger than several absorption and spin-diffusion lengths in the semiconductor, and the latter to leak from the HM surface.

The FEM calculations have been performed for a Pt/Ge junction, with $t_{Pt} = 4$ nm. The Ge thickness is set 70 µm, well above the typical absorption length of Ge, for $\hbar\omega > E_{dg}$ and the size of the mesh cell is less than 0.1 nm. The electron spin lifetime in Ge has been taken from typical values of Sec. **4**; the diffusion coefficient and mobility of Ge from Refs. [107, 108]; the absorption coefficient and the electron spin polarization of Ge from Refs. [109] and [69], respectively, as plotted in Fig. 16 (a). The dielectric constant of Ge is $\epsilon = 16.2\,\epsilon_0$, with ϵ_0 being the vacuum permittivity and the height of the Schottky barrier is $\phi_{bar} = 0.63$ eV (experimentally measured in Ref. [100]). Concerning the spin-diffusion length in Pt, values of ℓ_s^{Pt} ranging from 0.5 nm and 14 nm have been reported in the literature [110, 111, 112, 113]. However, it has been recently demonstrated that ℓ_s^{Pt} strongly depends on the thickness of the Pt layer [104, 114]: therefore, based on the findings of Ref. [114], we set $\ell_s^{Pt} = 1$ nm for a Pt thickness of 4 nm.

The results of the FEM calculations are reported in Fig. 11. In panels (a,b), we show the spatial dependence of the spin density $s(z)$, and of the spin current density $j_s(z)$, normalized to the photon flux, for $N_d = 2\times10^{16}$ cm^{-3}, and $\hbar\omega = 0.8$ eV. In panels (c-e) we compare the results of the spin current density injected into Pt $j_{s,0} = j_s(z = 0)$ resulting from the FEM model (blue dots), and from the Spicer-like formula [orange dots, eq. (23)]. The latter always overestimates $j_{s,0}$ since it neglects the built-in electric field

of the junction, which reduces the number of the injected spin-polarized electrons into the Pt layer. In Fig. 11 (c) we report the dependence of $j_{s,0}$ as a function of the doping concentration of Ge. A good agreement between the estimations of the two models is obtained for low doping concentrations (up to few 10^{16} cm^{-3}), while the models differ of more than a factor 3 for $N_d > 10^{17}$ cm^{-3}. Nevertheless, at a fixed doping density ($N_d = 2 \times 10^{16}$ cm^{-3}), we obtain a similar trend of the photon energy dependence of $j_{s,0}$ [Fig. 11 (d)] and the models differ only for a proportionality factor which can be inferred from Fig. 11. This demonstrates that the Spicer-like model produces consistent results if the amplitude of the signal is not considered. Since in eq. (23) the absorption coefficient and the electron spin polarization are known parameters, whereas the photon flux can be easily obtained, the photon energy dependence allows estimating the ℓ_s in the semiconductor, apart from the multiplicative constant ξ, which in any case does not affect the dependence of $j_{s,0}$ as a function of the incident photon energy.

Finally, in Fig. 11 (e) the dependence of $j_{s,0}$ on the spin-diffusion length in the Pt layer ℓ_s^{Pt} is shown. The Spicer-model is insensitive to this parameter, while the FEM model predicts a decrease of the spin current injected into the HM as ℓ_s^{Pt} increases. This discrepancy reflects the fact that, when ℓ_s^{Pt} is comparable with the thickness of the Pt layer, the boundary condition $s(z = 0) = 0$ of the Spicer-like model does not

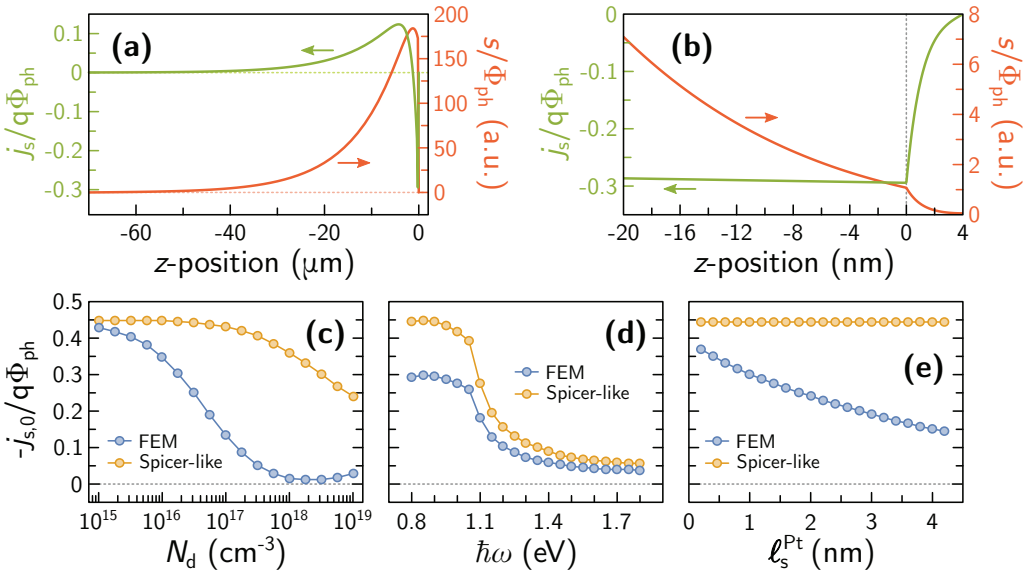

Figure 11.: (a,b) Spatial dependence of the spin current density j_s (green line) and the spin density s (red line), normalized with respect to the photon flux Φ_{ph}, resulting from FEM calculations. In this case we consider $N_d = 2 \times 10^{16}$ cm^{-3}, and $\hbar\omega = 0.8$ eV. (a) Spatial dependence of j_s and s within the whole investigated region. (b) Zoom close to the Pt layer. (c-e) Comparison of the spin current density injected into the Pt layer, calculated with the Spicer-like model (orange dots) and FEM analysis (blue dots). (c) Dependence on the doping concentration N_d of Ge at $\hbar\omega = 0.8$ eV. (d) Dependence as a function of the photon energy $\hbar\omega$ for $N_d = 2 \times 10^{16}$ cm^{-3}. (e)Dependence of the spin-diffusion length in Pt ℓ_s^{Pt} for $N_d = 2 \times 10^{16}$ cm^{-3}, and $\hbar\omega = 0.8$ eV. Figure reproduced from Ref. [145]

hold anymore. The decrease of $j_{s,0}$ with increasing ℓ_s^{Pt} is caused by the flow of the spin-polarized electrons which are reflected when they reach the Pt surface.

6. – Experimental techniques: charge-to-spin conversion

In the conventional magneto-optical Kerr effect (MOKE), the polarization of a light beam reflected by a magnetic medium is modified, depending on the magnetization state of the reflecting layer. Notably, the effect is still present even in media without a long-range magnetic order, but where an accumulation of spin-polarized carriers is present. By means of this technique Kato et al. [48] performed the first experimental demonstration of the SHE, directly imaging the spin accumulation in III-V microstructures. Up to now, similar investigations have been carried on in several semiconductors [115, 116] and metals [117, 118].

In what follows we investigate common schemes for MOKE detection of the electrically-induced spin accumulation given by the SHE.

6˙1. *MOKE experimental setup.* – The geometry of MOKE is shown in Fig. 12. A linearly polarized light beam impinges on the sample surface with a polar angle ϑ_0: the presence of a longitudinal (M_L), polar (M_P) or transverse (M_T) magnetization of the sample can provide for the rotation of the light polarization and the generation of an elliptic component of the reflected beam, accounted in the Kerr rotation ϑ_k and the Kerr ellipticity ε_k [119, 120]. Since the Kerr signal is usually quite small, the signal-to-noise ratio can be enhanced by modulating the light reflected from the sample with a PEM, as sketched in the experimental setups of Fig. 13. In this case, a Wollaston prism can be placed after the PEM to split the p and s components of the beam (see Fig. 13 (a)). Therefore, the detection with a balanced photodiode (BPD) allows one to measure the difference between the intensities of the two beams. This is the experimental geometry employed for the investigation of polar MOKE (P-MOKE).The linearly-polarized light beam impinges on the sampe at normal incidence and the reflected beam is divided by a beam-splitter (BS) to simultaneously measure the reflectivity of the beam by a single photodiode (PD-R) and the Kerr signal by means of the BDP. Alternatively, a

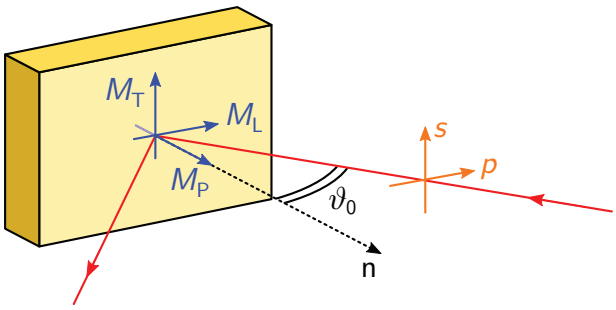

Figure 12.: Geometry of the MOKE. A laser beam shines a magnetized sample with a polar angle ϑ_0. The polarization state of the reflected light is varied compared to the light beam due to the magnetization of the sample. MOKE is defined as polar, longitudinal or transverse depending on the magnetization state of the sample M_P, M_L, and M_T, respectively.

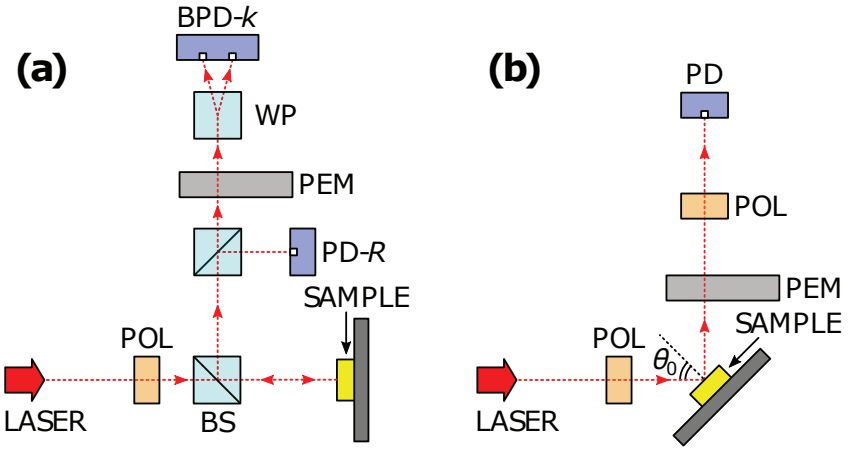

Figure 13.: Sketch of the experimental setup for P-MOKE (a) and L-MOKE (b). A linearly polarized laser beam illuminates the sample and the modulation of the reflected light with a PEM allows detecting either the ellipticity or the rotation of the reflected beam. To transform the modulation of the polarization in an modulation of the light intensity, the beam passes through a second polarizer and is detected with a photodiode.

second polarizer can be placed after the PEM, transforming the modulation of the light polarization, given by the PEM, in a modulation of the light intensity and allowing for the detection of the modulated Kerr signal with a photodiode (PD) (see Fig. 13 (b)). This is the experimental configuration exploited to investigate the longlitudinal MOKE (L-MOKE). In both PD and BPD schemes, the detected signal is demodulated with a lock-in amplifier.

6˙2. *Electrically-induced spin accumulation.* – The spin accumulation due to SHE can be detected with MOKE, in a stripe of geometrical dimensions d_x, d_y and d_z. Let us suppose that in our reference system [see, e.g., Fig. 7 (b)] a charge current density j_y flows along the y axis, as a result of the application of an electric field $\mathbf{E} = E_y\,\mathbf{u}_y$, being $\mathbf{u}_y$ the unit vector of the y axis. Due to SHE, a spin current density $j_{s,x}$ flows along the x axis [see eq. (1)], with the direction of the spin polarization along z (and thus detectable with P-MOKE), and similarly a spin current density $j_{s,z}$ flows along the z axis with the spin polarization of the carriers directed along x (and thus detectable with L-MOKE). In the following, we focus on the former case, the extension to the latter being straightforward. The estimation of the spin accumulation comes from the solution of the continuity and drift-diffusion equations for charge and spin. The charge and spin current densities flowing along x in presence of SHE are written as [121]:

$$j_x = q\left(D\,\frac{\partial n}{\partial x} + \mu_t s E_y\right), \tag{27a}$$

$$j_{s,x} = q\left(D\,\frac{\partial s}{\partial x} + \mu_t n E_y\right), \tag{27b}$$

where we have defined the *transverse mobility* $\mu_\mathrm{t} \triangleq \gamma\mu$. By exploiting the spin and charge continuity equations, under steady state conditions we get:

$$\frac{\partial^2 n}{\partial x^2} + \frac{\mu_\mathrm{t}}{D}\frac{\partial s}{\partial x}E_y = 0. \tag{28a}$$

$$\frac{\partial^2 s}{\partial x^2} + \frac{\mu_\mathrm{t}}{D}\frac{\partial n}{\partial x}E_y = \frac{s}{{\ell_\mathrm{s}}^2}. \tag{28b}$$

Since no charge current is flowing along x, we can impose $j_x = 0$ and obtain:

$$\frac{\partial n}{\partial x} = -\frac{\mu_\mathrm{t}}{D}sE_y, \tag{29}$$

which, substituted into eq. (28b), gives:

$$\frac{\partial^2 s}{\partial x^2} = s\left(\frac{1}{{\ell_\mathrm{s}}^2} + \frac{{\mu_\mathrm{t}}^2}{D^2}{E_y}^2\right). \tag{30}$$

The solution of this differential equation can be found by exploiting the boundary conditions $j_{\mathrm{s},x}(x = \pm d_x/2) = 0$. To obtain the carrier concentration n, we exploit the general solution of eq. (30) to solve eq. (28a), by imposing $j_x = 0$ and $n(x = 0) = n_0$. Finally, at the first order in E_y, the spin accumulation and the spin current density result, respectively [48, 121, 117, 116]:

$$s(x) = -\frac{\mu_\mathrm{t}}{D}\ell_\mathrm{s} n_0 \,\mathrm{sech}\left(\frac{d_x}{2\ell_\mathrm{s}}\right)\sinh\left(\frac{x}{\ell_\mathrm{s}}\right)E_y, \tag{31a}$$

$$j_{\mathrm{s},x}(x) = q\mu_\mathrm{t} n_0\left[1 - \mathrm{sech}\left(\frac{d_x}{2\ell_\mathrm{s}}\right)\cosh\left(\frac{x}{\ell_\mathrm{s}}\right)\right]E_y. \tag{31b}$$

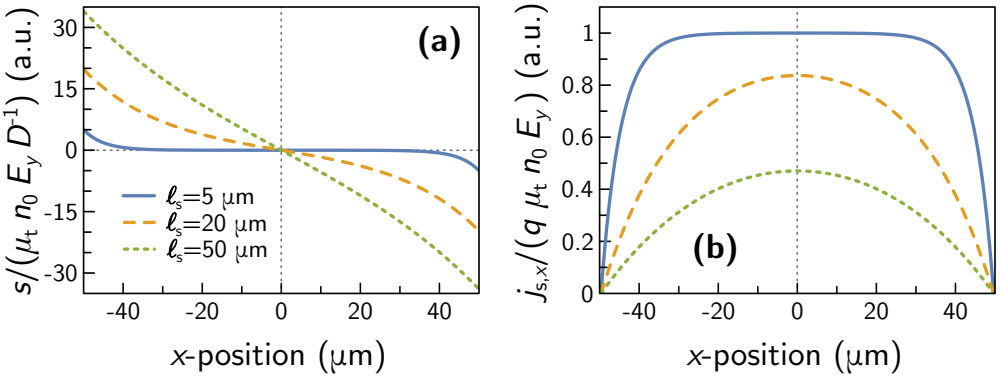

Figure 14.: Electrically-induced spin accumulation (a) and spin current density (b), normalized to the parameters in eqs. (31), expected in a stripe of width $d_x = 100$ μm for $\ell_\mathrm{s} = 5$ μm (blue line), $\ell_\mathrm{s} = 20$ μm (orange line), and $\ell_\mathrm{s} = 50$ μm (green line).

In Fig. 14 we report a sketch of the profiles of $s(x)$ and $j_{s,x}(x)$ in a stripe with $d_x = 100$ µm and with ℓ_s ranging between 5 µm and 50 µm. As ℓ_s increases, the spin accumulation at the edges of the stripe increases. When ℓ_s approaches $d_x/2$, the spin profile becomes linear. The spin current density at $x = 0$ decreases for increasing values of ℓ_s since the spatial distribution of the spin-polarized carriers generates a diffusive currents $\propto \partial s/\partial x$ which partially balances the SHE contribution [see eq. (27b)].

7. – Experimental results

7˙1. *ISHE in Pt/Semiconductor junctions.* – The spin transport in different HM/semiconductor junctions have been investigated, where HM is represented by a 4 nm-thick Pt layer, acting as a spin detector, whereas spins are optically injected in Ge, GaAs and Si substrates, with a thickness varying between 350 and 500 µm, well above the spin-diffusion length ℓ_s and the absorption length $\ell_\alpha = 1/\alpha$ of the semiconductors. The Pt film is grown on the (001) surface of the semiconductors. Substrates are n-doped (with As for Ge, P for Si, and Si for GaAs), with dopant concentration $N_d^{Ge} = 1.6 \times 10^{16}$ cm^{-3}, $N_d^{Si} = 9 \times 10^{14}$ cm^{-3} and $N_d^{GaAs} = 2 \times 10^{18}$ cm^{-3}.

We illuminate Pt/Ge, Pt/Si, and Pt/GaAs junctions at grazing incidence (spotsize $\approx$ 10 µm) to photogenerate an in-plane component of the spin polarization in the CB of semiconductors. Spins diffuse to the thin Pt layer, where the ISHE takes place. The voltage difference resulting from the conversion of the spin current into a charge current is detected under open circuit conditions by means of two ohmic contacts (200 nm-thick Au/Ti) grown on the top of the Pt layer, as sketched in Fig. 7 (a). All the measurements are performed at room temperature.

7˙1.1. *Signal characterization.* Fig. 15 shows the ISHE signal in the Pt/Ge sample as a function of the polar ϑ and azimuthal φ angles, the DCP and the incident optical power W. The measurements are acquired with a photon energy resonant with the Ge direct gap $\hbar\omega = 0.8$ eV. In Fig. 15 (a,b), the angular dependences of the detected signal confirm the linear dependence for small polar angles ϑ and a cosine dependence on the azimuthal angle

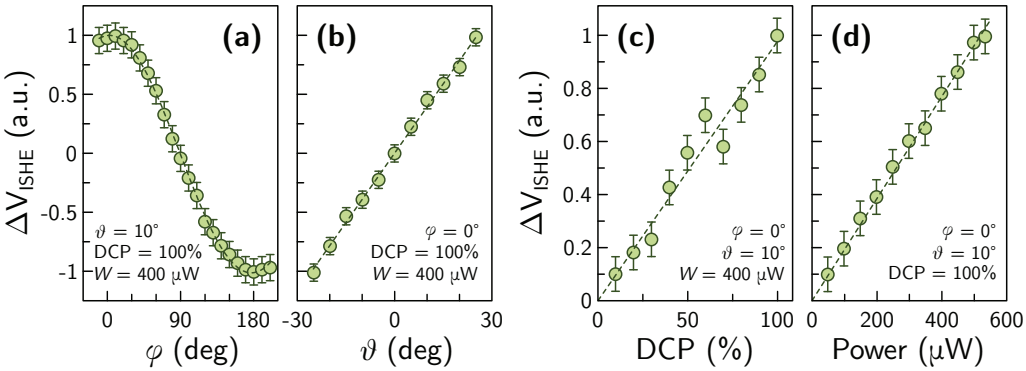

Figure 15.: Dependences of ISHE signal in a Pt/Ge sample for $\hbar\omega = 0.8$ eV as a function of (a) the azimuthal φ and (b) polar ϑ (b) angles. ISHE signal as a function of (c) the DCP and (d) the optical power, incident on the sample. Dashed lines show a fit of the experimental data based on eq. (18).

φ, expected for a photoinduced ISHE signal [see eq. (18)]. For comparison, theoretical predictions are reported in Fig. 9. The linearity of the detected signal with the DCP is reported in Fig. 15 (c). In Fig. 15 (d), we show the linear dependence of the signal with the optical power density impinging on the sample, as expected from eq. (18). These results confirm the spin-related nature of the detected signal. Similar characterizations have been carried on for the Pt/Si and Pt/GaAs samples.

7˙1.2. *Photon energy dependence.* In Sec. **3**, we have detailed the physics of the optical orientation process in Ge. As already mentioned, the discussion can be applied to GaAs in a straightforward manner, by considering the different bandstructure parameters: $E_{\mathrm{dg}}^{\mathrm{GaAs}} \approx 1.42$ eV, and $\Delta_0^{\mathrm{GaAs}} \approx 0.32$ eV. Both in Ge and in GaAs, SOI is strong enough to induce a significant splitting of the HH and LH bands from the SO one.

Optical orientation in Si is quite different: SOI is small ($\Delta_0^{\mathrm{Si}} \approx 0.04$ eV) and the direct band gap is in the ultraviolet range ($E_{\mathrm{dg}}^{\mathrm{Si}} \approx 3.4$ eV), while the bottom of the CB lies along the Δ direction, and $E_{\mathrm{ig}}^{\mathrm{Si}} \approx 1.12$ eV. Thus, at variance with Ge and GaAs, where a direct (or quasi-direct in the case of Ge) gap is present and optical transitions occur around Γ, optical spin injection in Si is performed by exploiting indirect $\Gamma \rightarrow \Delta$ transitions with circularly polarized light, mediated by phonons. This mechanism has been predicted theoretically in Ref. [71]. In this case, the maximum $P_{\mathrm{n},0}^{\mathrm{Si}}$ that can be obtained at room temperature is about 5%, rapidly decreasing as the photon energy is increased above $E_{\mathrm{ig}}^{\mathrm{Si}}$.

After photogeneration, spins diffuse towards the Pt layer. At variance from Ge and Si, GaAs is a direct gap semiconductor. In GaAs, both generation and transport occur at Γ. In Ge, the electrons photoexcited at Γ undergo a fast $\Gamma \rightarrow L$ scattering (mostly spin-preserving, see Sec. **4**, and Ref. [122]), the transport occurring at the L minima. Finally, in Si the spin-polarized electrons are directly photogenerated in Δ, where also spin transport takes place.

In Fig. 16, we report the experimental photon energy dependence of the ΔV_{ISHE} signal in the case of Pt/Ge, Pt/Si, and Pt/GaAs, for $\varphi = 0°$, and $\vartheta = 10°$. To account for the different optical power impinging on the sample, the ISHE signal is normalized to the photon flux Φ_{ph} transmitted to the substrate, obtained by means of the optical analysis reported in Sec. **5**˙2.1.

Phenomenologically, the ISHE signal for the Pt/Ge sample has its maximum when the photon energy is tuned around $E_{\mathrm{dg}}^{\mathrm{Ge}}$ and then decreases as transitions towards the SO band are allowed. Thus, ΔV_{ISHE} nicely mimics the initial spin polarization of the electrons, shown in Fig. 4, and for convenience reported in Fig. 17 (a). On the contrary, in the case of Si and GaAs, ΔV_{ISHE} is quite small at the energy gap and increases as a function of the photon energy, up to a plateau. This behavior is radically different from the spin polarization at the generation time shown in Fig. 17 (b,c) for Si and GaAs, respectively.

The experimental results of Fig. 16 can be interpeted within the frame of the Spicer-like model. We modify eq. (23) to explicitly account for the absorption and spin-diffusion lengths:

$$\Delta V_{\mathrm{ISHE}} \propto P_{\mathrm{n},0} \frac{\ell_{\mathrm{s}}/\ell_\alpha}{1 + \ell_{\mathrm{s}}/\ell_\alpha}. \tag{32}$$

Hence, the detected signal is determined by the initial spin polarization $P_{\mathrm{n},0}$, and by the ratio between the absorption length $\ell_\alpha = 1/\alpha$ and the spin-diffusion length ℓ_{s} of the semiconductor. Since the photon energy dependence of both $P_{\mathrm{n},0}$ and the absorption

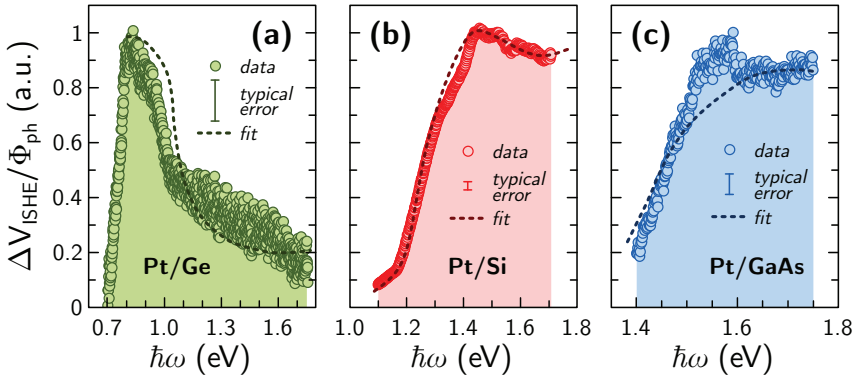

Figure 16.: Detected ISHE signal for $\varphi = 0^\circ$, and $\vartheta = 10^\circ$, normalized to the photon flux Φ_{ph}, as a function of the photon energy for (a) Pt/Ge, (b) Pt/Si, and (c) Pt/GaAs junctions. The dark dotted lines show the fit of the data with the 1D drift-diffusion Spicer-like model [eq. (23)].

coefficient α are well established in the literature, the fit of the experimental data provides an estimation of the spin-diffusion length in the investigated semiconductors. Here, we assume that the value of ℓ_s does not depend on the photon energy. However, this is a valid assumption only if the spin-polarized electrons relax at the bottom of the CB, preserving the spin character, i.e., if spins are scattered at the bottom of the CB within a time scale much faster than the electron spin lifetime [73]. Indeed, this condition holds when photon energy is close to the gap of the semiconductor.

The different behavior of ΔV_{ISHE} as a function of the photon energy in Ge, compared to Si and GaAs, can be ascribed to the different ℓ_s/ℓ_α ratio. Indeed, if we evaluate eq. (32) in the limiting case $\ell_s \gg \ell_\alpha$, we get $\Delta V_{ISHE} \propto P_{n,0}$, while $\ell_s \ll \ell_\alpha$ produces $\Delta V_{ISHE} \propto \alpha P_{n,0}$. Since the ISHE signal in Pt/Ge mimics the initial spin polarization of Ge, the Spicer-like model predicts $\ell_s^{Ge} > \ell_\alpha^{Ge}$. On the contrary, we expect $\ell_s < \ell_\alpha$ for Si and GaAs, thanks to the small spin lifetime in the case of GaAs due to the Dyakonov-Perel spin relaxation mechanism [50], and to the long absorption length in Si related to the absence of direct transitions within the explored energy range.

The photon energy dependence of the normalized ISHE signal, according to the Spicer-like model [eq. (32)], is shown in Fig. 17 (d-f) for different values of ℓ_s. In Fig. 17 (a-c) we show the initial electron spin polarization and the absorption coefficient used for the calculations. Consistently with the previous discussion, by comparing the calculations of Fig. 17 with the experimental results in Fig. 16, high values of ℓ_s (in units of ℓ_α) better fit the results of Ge, while the opposite applies for Si and GaAs.

The best fit of the experimental results yields $\ell_s^{GaAs} = 30 \pm 5$ nm and $\ell_s^{Si} = 9 \pm 2$ µm for GaAs and Si, respectively. For Ge, the Spicer-like model only provides a lower bound estimation of the electron spin diffusion length, since similar spectra are obtained for values of ℓ_s^{Ge} larger than 1 µm. The estimated ℓ_s values are in agreement with those reported in the literature, either for GaAs [125, 93], Si [71, 126, 127] or Ge [128, 31, 129, 97].

The evaluation of the amplitude of the ISHE signal in Pt/Semiconductor junctions is a critical issue. Indeed, if we analyze ΔV_{ISHE} at the Ohmic contacts for the Pt/Ge sample, measured for $\hbar\omega = 0.8$ eV, we get an ISHE charge current inside the illuminated

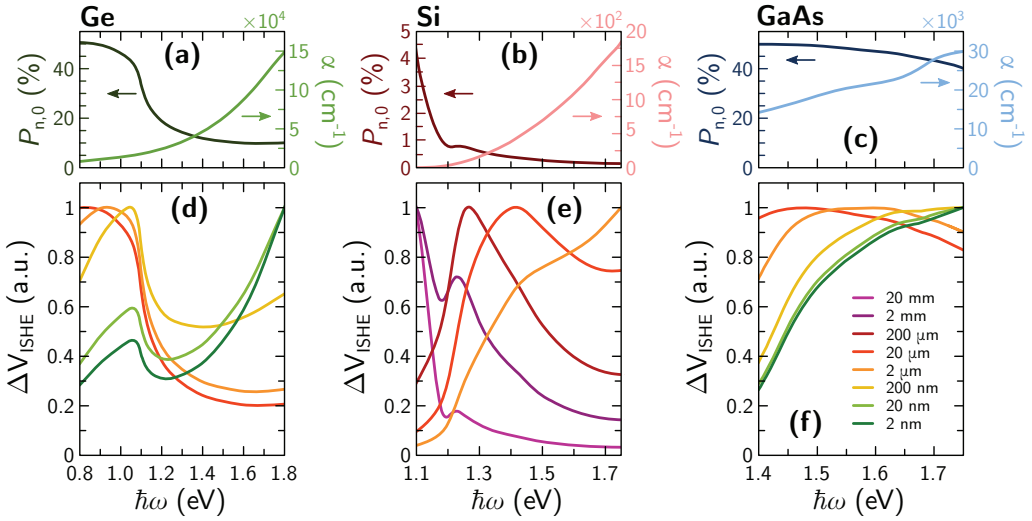

Figure 17.: The top panels (a-c) show the initial electron polarization (dark line) and absorption coefficient (light line) for Ge (a, from Refs. [69] and [109], respectively), Si (b, from Ref. [71]), and GaAs (c, from Refs. [123] and [124], respectively). The bottom panels (d-f) show the trend of the ISHE spectra obtained with a 1D drift-diffusion model, for different values of ℓ_s in the case of a Pt/Ge (d), Pt/Si (e), and Pt/GaAs (f) junction (Ref. [100]). The color scale of the spin-diffusion lengths is reported in panel (f).

region, normalized to $q\,\Phi_{ph}$, equal to $j_{ISHE}/q\,\Phi_{ph} \sim 10^2$ [see Sec. **5**˙2]. At the same time we can calculate the optically injected spin current density, normalized to $q\,\Phi_{ph}$, obtaining $j_s/(q\,\Phi_{ph}) \sim 10^{-2}$. Therefore, $\gamma = j_{ISHE}/j_s \sim 10^4$ [see eq. (26)], which yields an unphysical result for the SCI efficiency in Pt. Despite effective spin-Hall angles larger than unity have been estimated by measuring the spin-orbit torque exerted by topological surface states on ferromagnets [130, 131, 132, 133, 134], the above value of the SCI efficiency is roughly five orders of magnitude larger than the commonly accepted value $\gamma \approx 0.1$ [135, 136, 111, 137, 138]. Such a discrepancy could be due to the fact that the Spicer-like model does not consider the possible presence of some spin enhancement mechanism operating in Pt [139] or at the Pt/semiconductor interface, where photovoltaic effects related to the in-plane electrons diffusion can also play a major role [140, 141, 142].

7˙2. *Non-local spin injection/detection scheme in Ge.* – In Fig. 18 we show the structure of the sample and the scheme of measurements. We employ a series of Pt pads, grown on top of a As-doped Ge(001) substrate (doping concentration $N_d^{Ge} = 1.6 \times 10^{16}$ cm^{-3}), to generate an in-plane component of the spin polarization of the photogenerated electrons, as explained in Sec. **5**˙1, by locally illuminating with a focused laser beam ($\hbar\omega =$ 0.8 eV). Optically injected spins diffuse in the Ge substrate toward the detection point. The detection is performed via ISHE taking place in a Pt stripe with two Au(250 nm)/Ti(10 nm) Ohmic contacts grown on the top [Fig. 18 (b)]. The spin-dependent signal, together with the sample reflectivity, is recorded as a function of the focused beam position. All the measurements have been acquired at room temperature.

Figure 19 shows the experimental results. In panels (a-c), we report the dataset

for the sample described in Fig. 18, while panels (d-f) show the results for a similar sample, where the detection is performed with a magnetic tunnel junction (MTJ)

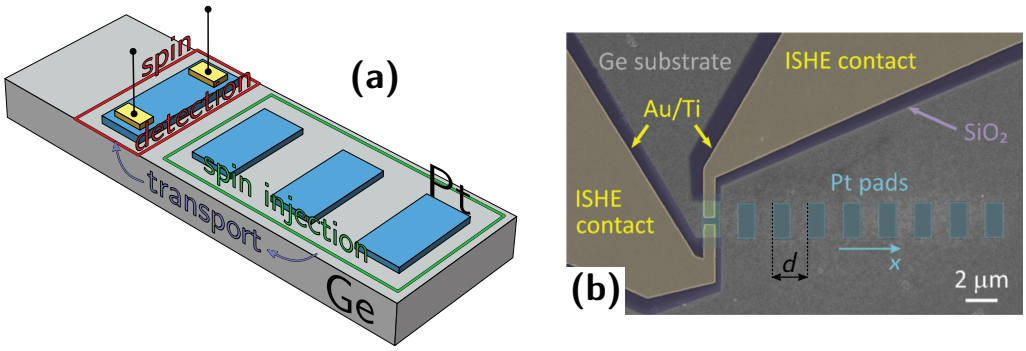

Figure 18.: (a) Scheme of the non-local spin injection/detection scheme. We employ a series of Pt stripes to generate an in-plane component of the spin polarization via optical orientation. Spin-polarized photoelectrons transported in Ge to the detection point, operated via ISHE in an additional Pt stripe. (b) Scanning electron microscope image of the sample, from Ref. [32]. Pt pads are 1×2 µm^2-wide and the spacing between pads along the x axis is 1 µm, so that the periodicity is $d = 2$ µm.

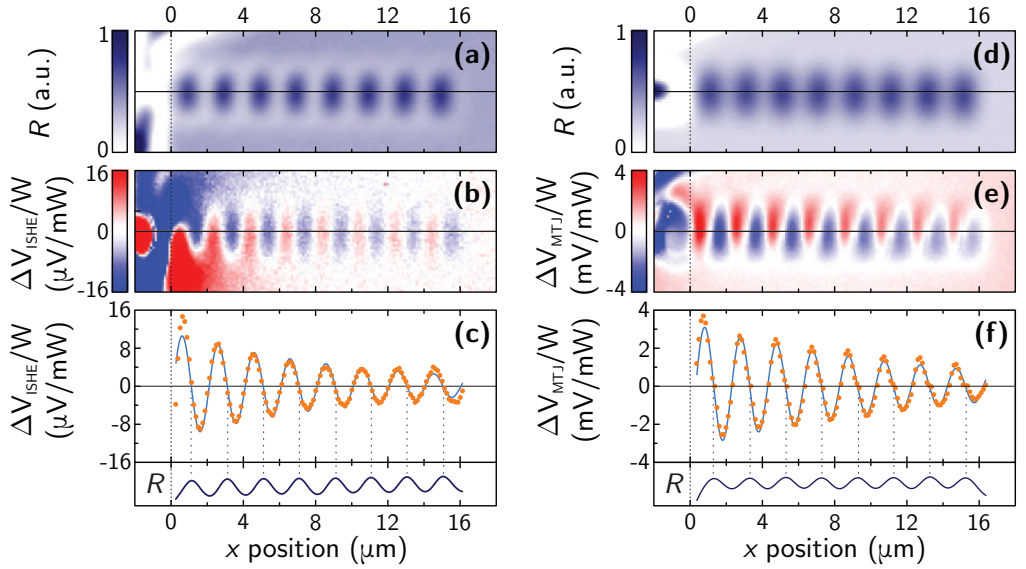

Figure 19.: (a,d) Reflectivity image of the ISHE and MTJ devices, respectively. (b,e) Map of the spin-dependent electrical signal, normalized to the incident optical power (900 µW and 60 µW for ISHE and MTJ, respectively) at $\hbar\omega = 0.8$ eV. (c,f) Profiles of the (a,b,d,e) maps taken at the center of the Pt pads, as a function of the distance x from the detector. The orange dots show the experimental data, whereas the light blue line represents the fitting with a 1D diffusion model [32].

rather than via ISHE in Pt, to validate the results obtained with the ISHE detection scheme. In Fig. 19, ΔV_{MTJ} is the potential difference acquired between an Ohmic contact [Au(250 nm)/Ti(10 nm)], deposited on top of the Ge surface, and a second contact grown on the top of the Pt(5 nm)/Fe(15 nm)/MgO(3.5 nm) MTJ. In this sample, a 3.5 nm-thick MgO layer has also been deposited between the Pt generation pads and Ge. To compare the results of ISHE and MTJ detection, we force the magnetization of the Fe layer to lie along the x axis in Fig. 18 (b). In this way, both spin-detection schemes are sensitive to the x direction of the spin polarization.

In Fig. 19 (a,d) the reflectivity of the samples is reported. The spin-related electrical signal is shown in Fig. 19 (b,e), normalized to the optical power density illuminating the sample. Since we are able to correlate the spin generation point to the corresponding detected signal, this spin injection/detection schemes allow for a direct measurement of the diffusive spin paths in Ge. Opposite signals are detected when the laser beam illuminates opposite edges of Pt pads. Notably, the amplitude of the signal decreases by moving the light beam away from the detection point, as a consequence of the spin depolarization due to diffusion in Ge. In Fig. 19 (c,f) the orange dots represent the voltage signal recorded at the center of the Pt stripes, as a function of the distance from the spin detector along the x axis, while the dark blue profile corresponds to the reflectivity along the same axis. The electrical signal is zero at the center of the Pt pads and is reversed at the two opposite edges.

The experimental results can be interpreted within the frame of a 1D diffusion model [143], acording to which:

$$\Delta V(x) \propto \sin(2\pi x/d)\, e^{-x/\ell_{\mathrm{s}}}, \tag{33}$$

where the sinusoidal term accounts for the periodicity of the spin generation, being $d = 2$ µm the periodicity of Pt pads along the x axis, and $x = 0$ the position of the detector. Since, by measuring ΔV as a function of the distance, we observe a relative variation of the spin-related signal, the only free parameter in eq. (33) is the spin-diffusion length ℓ_{s}. The light blue curve in Fig. 19 (c,f) reports the results of the fitting, which yield $\ell_{\mathrm{s}}^{\mathrm{ISHE}} = 10 \pm 1$ µm and $\ell_{\mathrm{s}}^{\mathrm{MTJ}} = 12 \pm 1$ µm, for ISHE and MTJ devices, respectively. We ascribe the difference in ℓ_{s} to the thin MgO layer below the Pt pads for the spin generation in the MTJ device. This prevents most of the absorption of the spins from the Pt pads between the generation and detection point, which act as an effective spin relaxation channel.

The measured value of $\ell_{\mathrm{s}} \approx 12$ µm yields a spin lifetime $\tau_{\mathrm{s}} \approx 20$ ns, if a diffusion coefficient $D = 65$ cm^{2}s^{-1} is employed [144, 145]. The experimentally estimated ℓ_{s} value is larger than what expected from the theoretical calculations carried on in Sec. **4** ($\tau_{\mathrm{s}}^{\mathrm{th}} \approx 5$ ns). However, for lightly n-doped samples, the most efficient spin relaxation channel is intervalley scattering (see Sec. **4** amd Ref. [31]), of which theoretical estimation suffers from a large variability of the relevant parameters, both in the calculations of Sec. **4** and in Refs. [31] and [77].

Finally, it is important to point out that, despite the higher responsivity of the MTJ detection block, the exploitation of ISHE allows realizing a spin injection/detection scheme without any ferromagnetic material. Moreover, at variance from other injection/detection schemes, the employed technique is able to probe the pristine interface of materials grown on the Ge surface. This can be particularly suitable in the investigation of topologically protected surface states where the surface quality is of crucial importance.

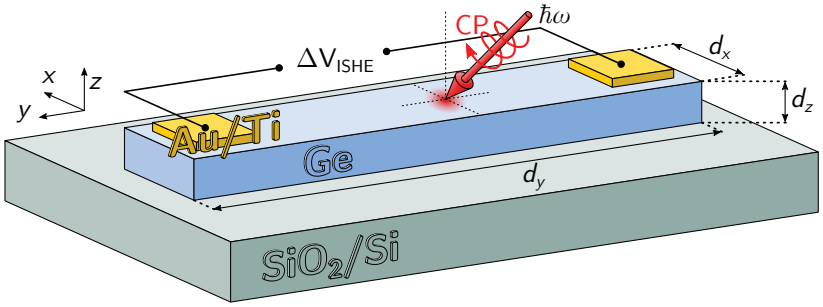

Figure 20.: Sketch of the sample for ISHE measurements directly in bulk Ge. A stripe of single crystal Ge lies on the top of a SiO_2/Si substrate. The geometrical dimensions of the stripe are $d_x \times d_y \times d_z = 1 \times 20 \times 1$ µm^3. A CP light beam illuminates the stripe at grazing incidence, thus photogenerating in the CB of Ge a spin-polarized electron population. The charge current resulting from ISHE in Ge is detected by measuring the potential difference under open circuit conditions ΔV_{ISHE} between two Au/Ti ohmic contacts.

7˙3. *Spin-to-charge conversion in Ge.* – As discussed above, the fundamental feature for an efficient spin detector is a non-negligible SOI. This is the reason why non-magnetic heavy metals such as Au or Pt are employed to detect spin currents. However, SOI in Ge is quite large, therefore it is also possible to induce SCI phenomena directly in Ge. In particular, it is convenient to optically generate a spin current in Ge, detecting the electric signal resulting from the ISHE directly in a Ge stripe. Figure 20 shows the layout of the sample. The Ge stripe is fabricated by employing the germanium-on-insulator (GOI) technique, realized with the Smart Cut process [146]. The obtained wafer consists of a 1 µm-thick Ge layer on a 1 µm-thick buried oxide. The uniform doping of the Ge layer has been obtained via multiple ion implantations at different energies. To evaluate the SCI of bulk Ge as a function of the doping type, we investigate a n-doped sample (P-doped, $N_{\mathrm{d}} = 2 \times 10^{19}$ cm^{-3}) and a p-doped one (B-doped, $N_{\mathrm{a}} = 5 \times 10^{18}$ cm^{-3}). Indeed, since the spin-Hall angle of Ge is expected to be quite low for thermalized electrons [90], by decreasing the electrical resistivity the skew scattering conductivity is supposed to increase [50]. The measured resistivity for n- and p-type Ge are $\rho_n = 1.2$ mΩ · cm and $\rho_p = 3.9$ mΩ · cm, respectively. The Au(150 nm)/Ti(10 nm) ohmic contacts have been deposited in UHV on the clean Ge surface. Then, the sample has been lithographically defined in the geometry of Fig. 20.

Optical orientation has been performed by illuminating the sample at grazing incidence with a polar angle $\vartheta \approx 20°$ [see Fig. 7 (b)], corresponding to ϑ_{Ge} between 3.3° and 4.7° inside Ge within the explored range of photon energies. Throughout all the measurements, the azimuthal angle φ has been set at 0° to maximize the component of the spin polarization directed along the x axis.

In this case, we have employed a double modulation technique to increase the signal-to-noise ratio, by modulating the light CP at 50 kHz by means of the PEM and chopping the light intensity at 21 Hz.

Figure 21 shows the ISHE signal ΔV_{ISHE} for the analyzed samples, normalized to the photon flux Φ_{ph}. For both the samples, ΔV_{ISHE} changes sign around $\hbar\omega \approx 1.04$ eV, which corresponds to the onset of the transition from the SO branch in the Ge valence band

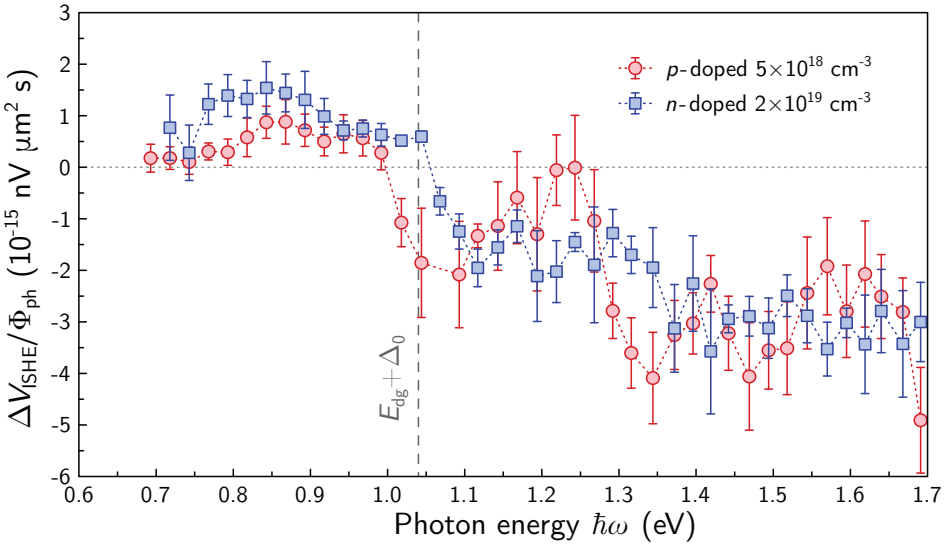

Figure 21.: ISHE signal for p- (red circles) and n-doped Ge (blue squares) samples. ΔV_{ISHE} has been normalized to the photon flux Φ_{ph}. Each data point represents the average value of ten acquisitions of 200 s each. Figure reproduced from Ref. [73].

at $E_{\mathrm{dg}} + \Delta_0 = 1.09$ eV. The slight energy difference is given by the band gap narrowing occurring in heavyly-doped Ge samples [147].

The sign inversion depends on the interplay between the spin and the energy relaxation times of the photoexcited electron population. To unravel the physical mechanism determining the ISHE signal, it is necessary to analyze the spin relaxation mechanisms in the Ge conduction band and the temporal dependence of the electron spin polarization $P_{\mathrm{n}}(t)$. To this purpose, Fig. 22 reports the momentum τ_{m}, energy τ_{ϵ} and spin τ_{s} relaxation times of the photoexcited electrons in the investigated samples, based on the analysis performed in Secs. **4**. It is possible to see that at low kinetic energies ($E_{\mathrm{k}} < 0.45$ eV) the energy relaxation time is shorter than the spin lifetime [see Fig. 22 (a)]. Therefore, within this energy range, spin is preserved and energy is thermalized. On the contrary, for higher kinetic energies ($E_{\mathrm{k}} > 0.45$ eV), the spin depolarization occurs before energy thermalization. Therefore, we can conclude that the interplay between spin relaxation and momentum and energy relaxation is the driving mechanism for the experimentally observed sign inversion.

Figure 23 shows snapshots of the calculated electron spin polarization at three different times after photogeneration. To calculate $P_{\mathrm{n},0}(\hbar\omega)$, we employ standard matrix elements for the optical transitions at the Γ point and we take into account a simplified JDOS resulting from a parabolic band approximation around Γ, as shown in Sec. **3**. Thanks to the energy conservation, we can infer the energy distribution of the different spin populations photoexcited from the HH, LH, and SO branches [148], which are evidently affected by different spin and energy relaxation times as a function of their kinetic energy [see Fig. 22]. As a consequence, the temporal evolution of the spin polarization,

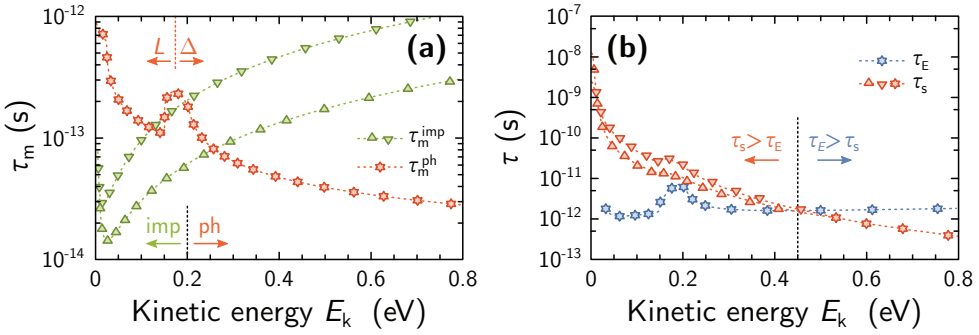

Figure 22.: (a) Kinetic energy dependence of momentum scattering time. The red stars represent the momentum relaxation time given by phonons, whereas green triangles [upwards (downwards) for the $n(p)$-doped sample] the one related to impurities. The red vertical lines indicate the crossover between the region of the phonon scattering by inter-LL-valley and inter-$\Delta\Delta$-valley scattering. The dark vertical line separates the regions of impurity- or phonon-driven momentum scattering. (b) Spin (red) and energy (blue) lifetimes. The meaning of the symbols is the same as in panel (a). The vertical line at E_k shows the crossover between τ_s and τ_E. Figure reproduced from Ref. [73].

defined as

$$P_n(t) = \frac{n_\uparrow(t) - n_\downarrow(t)}{n_\uparrow(0) + n_\downarrow(0)}, \tag{34}$$

depends on the photon energy and can be obtained by calculating the time evolution of the three photoexcited populations.

Bearing in mind Fig. 23, at $t = 0$ the spin polarization is determined by the electrons originated from the HH, which are the majority of the photoexcited electrons. However, the latters are promoted at higher energies compared to the ones originated from the SO

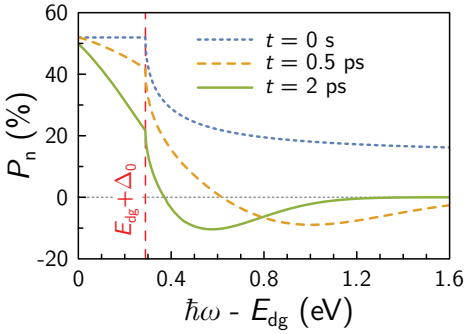

Figure 23.: Spin-polarization spectra of the photogenerated electrons at the generation time ($t = 0$, blue dotted line), at 0.5 ps and 2 ps (orange dashed and green continuous lines, respectively). Figure reproduced from Ref. [73].

branch, so that they undergo to a faster depolarization. Thus, when transitions from the SO states are allowed, a sign reversal of the polarization occurs after a finite time interval.

Finally, we derive ΔV_{ISHE} directly from the ISHE relation [eq. (2)]. Since $|\mathbf{j}_{\mathrm{s}} \times \mathbf{u}_{\mathrm{s}}| = j_{\mathrm{s}} \sin(\vartheta_{\mathrm{Ge}})$, the-time dependent potential difference at the ohmic contacts reads:

$$\Delta V_{\mathrm{ISHE}} = \gamma \left\langle j_{\mathrm{s}}(z) \right\rangle_z \rho \, d_z \, \sin(\vartheta_{\mathrm{Ge}}), \tag{35}$$

where $\left\langle j_{\mathrm{s}}(z) \right\rangle_z$ is the average of the spin current density $j_{\mathrm{s}}(z)$ over the stripe thickness d_z. The expression of $j_{\mathrm{s}}(z)$ comes from the spin-continuity and drift-diffusion equations in the steady state conditions ($\partial s/\partial t = 0$), with optical generation of a spin population [eq. (19)], resulting in the pure spin-diffusion equation [eq. (20)]. The equations are solved by imposing the boundary conditions $j_{\mathrm{s}}(0, -d_z) = 0$ to model the fact that spin cannot leak from the Ge layer at the Ge/air ($z = 0$) or Ge/SiO_2 ($z = -d_z$) interfaces. We then calculate $j_{\mathrm{s}}^{\mathrm{av}} = \left\langle j_{\mathrm{s}}(z) \right\rangle_z$ by averaging $j_{\mathrm{s}}(z)$ over the thickness d_z of the stripe. In Fig. 24 (a), we report the total spin current density $j_{\mathrm{s}}^{\mathrm{av}}$, and the partial contributions generated from the electrons promoted from HH, LH, and SO states. As already discussed for the time-dependence of the electron spin polarization [Fig. 23], electrons promoted from the SO band hold their spin character for a longer time compared to the electrons promoted from the HH band, as a consequence of the different spin relaxation times.

By comparing Figs. 21 and 24, one can notice that, despite the calculated spin current density nicely mimics the sign reversal, the trends of the measured ΔV_{ISHE} and the calculated $j_{\mathrm{s}}^{\mathrm{av}}$ are completely different. Since in eq. (35) all the parameters are measured or calculated except the spin-Hall angle γ of Ge, the different trend of ΔV_{ISHE} and $j_{\mathrm{s}}^{\mathrm{av}}$ reveals the energy dependence of γ. Therefore, we can directly estimate the SCI efficiency for n- and p-doped samples from eq. (35), obtaining the results presented in Fig. 25. The value of γ for thermalized electrons in the n-doped sample ($\approx 2 \times 10^{-4}$) is in good agreement with the one estimated from spin pumping in a CoFeB/MgO layer grown on top of a heavily P-doped Ge (doping concentration $N_{\mathrm{a}} \approx 10^{19}\mathrm{cm}^{-3}$) [90]. On the contrary, $\gamma \approx 2 \times 10^{-5}$ for thermalized electrons in p-type Ge, which is much lower

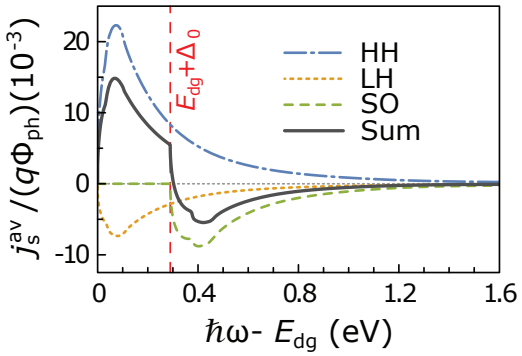

Figure 24.: Average of the total spin current density $j_{\mathrm{s}}^{\mathrm{av}}$ flowing in the Ge layer (gray continuous line) and partial contributions given by the populations promoted from HH (blue dash-dotted line), LH (orange dotted line), and SO (green dashed line). Figure reproduced from Ref. [73].

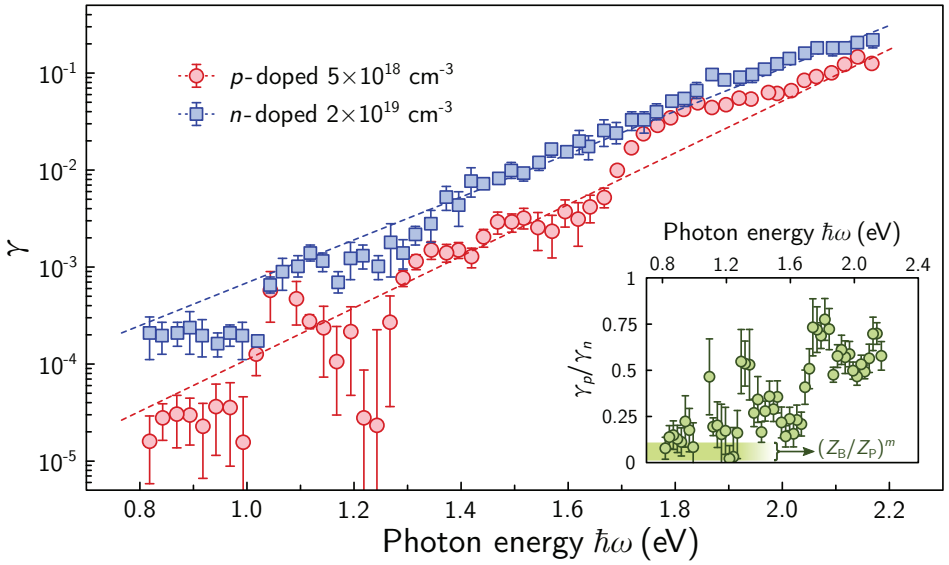

Figure 25.: Spin-Hall angle $\gamma_{n(p)}$ as a function of the photon energy for $n(p)$-doped Ge [blue squares (red circles)]. The inset shows the ratio γ_p/γ_n with the band marking the ratio of the spin-Hall angle estimated within an atomic model. The parameter m ranges between 2 and 4. Figure reproduced from Ref. [73].

than the value estimated from spin pumping measurements in a B-doped Ge sample ($N_\mathrm{d} \approx 10^{18}$ cm^{-3}) [149].

For thermalized electrons, scattering is mainly due to impurities [see Fig. 22 (a)], therefore we can employ a simple atomistic picture where the spin-dependent scattering cross section follows the atomic number of the scattering center $\propto Z^m$, with m ranging between 2 and 4. In this case, $\gamma_p/\gamma_n \approx (Z_\mathrm{B}/Z_\mathrm{P})^m \approx 0.01 - 0.11$, being Z_B and Z_P the atomic numbers of B and P, the dopants of p- and n-type Ge, respectively. From the experimental data $\gamma_p/\gamma_n \approx 0.1$, nicely falling in the range of the atomistic picture. The ratio between the spin-Hall angle for the p- and n-type Ge are reported in the inset of Fig. 25, together with the band marking the ratio obtained from the atomic picture.

It is worth noticing that in Fig. 21 the detected ΔV_ISHE signals are comparable for n- and p-doped Ge, despite from Fig. 25 we infer $\gamma_n > \gamma_p$. This is due to the higher resistivity for p-doped Ge, which, from eq. (35), balances the higher spin-Hall angle of n-doped Ge. Figure 25 also suggests that the extracted γ value has roughly an exponential growth with $\hbar\omega$ for both dopants. For high photon energies we estimate $\gamma \approx 0.1$, a value much larger than the ones reported up to now for semiconductors [116, 150, 151, 152, 90, 153, 93]. Notably, a value of $\gamma = 0.02$ has been estimated in GaAs [152] for electrons with kinetic energies $E_\mathrm{k} \approx 0.3$ eV. Moreover, in that case an exponential growth with E_k has been also reported and ascribed to a higher occupation probability of the L valley of GaAs, where the SOI was expected to be larger. A similar increase of γ has also been observed in Ref. [93]. In both reports [152, 93], γ for thermalized electrons has been estimated between 2×10^{-4} and 5×10^{-4}. We can gain some more insight from the photon energy dependence of the ratio γ_p/γ_n, shown in the inset of Fig. 25. If for thermalized electrons the ratio is about 0.1, its value increases up to 0.8 at higher photon energies. From

the calculations of the momentum relaxation time [Fig. 22 (a)], we deduce that, at low $E_{\rm k}$, the momentum scattering is lead by collisions with impurities, while, as the kinetic energy increases, the phonon contribution becomes dominant. Indeed, the dependence of γ_p/γ_n on the photon energy seems to reflect this behavior. For near-gap excitations the ratio can be inferred from the atomistic picture of the cross section of the scattering from impurities. As the photon energy increases, the contributions from phonon scattering increases and no difference in n- and p-doped Ge is expected when the SCI is mediated by phonons. Thus, γ_p and γ_n approach the same value. Moreover, the paramount increase of γ with the photon energy suggests that phonon scattering is much more efficient compared to impurity scattering for SCI.

Finally, it is interesting to compare the results described above with the spin-to-charge conversion discussed for a Pt/Ge junction (Sec. **7**˙1). At variance with Fig. 21, in the case of Pt/Ge, the ISHE signal does not show any sign reversal as a function of the incident photon energy. To solve this discrepancy we can exploit the Spicer-like model [eq. (23)] to calculate the total spin current injected in the Pt layer from Ge, when three independent spin populations (promoted from HH, LH, and SO) are considered. The result is shown in Fig. 26, compared to the case of Ge. Notably, no sign reversal is expected in the spin current density injected into the Pt film, as experimentally observed in the Pt/Ge junction [Fig. 16 (a)]. The difference lies in the fact that, if electrons diffuse from Ge to Pt, their spin depolarization mostly occurs in the Pt layer, while for the ISHE in Ge all the spin relaxation takes place inside the semiconductor.

7˙4. *Spin-Hall effect in Ge.* – To completely characterize the spin-to-charge interconversion phenomena in Ge, the spin-Hall effect has to be taken into account. In this case, we investigate a 3 µm-thick Ge bar grown on a 500 µm-thick Si(001) substrate. Since electrons should flow only inside germanium to generate an electrically-induced spin accumulation, we employ P-doped Ge with a doping concentration $N_{\rm s} = 2.5 \times 10^{18}$ cm^{-3} (resistivity $\rho_{\rm Ge} = 10.5$ mΩ cm at 20 K), whereas the Si substrate is highly insulating ($\rho_{\rm Si} > 10$ kΩ cm). An optical image of the sample is shown in Fig. 27 (a). The Ge stripe has a size of $d_x \times d_y = 100 \times 220$ µm^2, along the x and y axes [within the reference frame of Fig. 27 (a)], respectively.

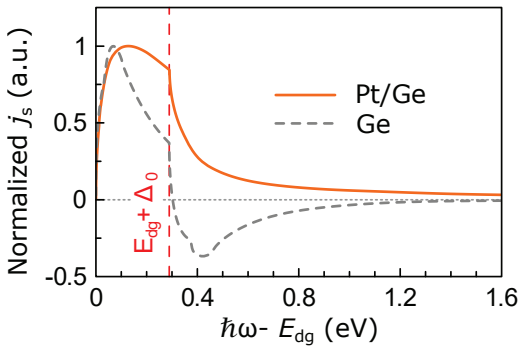

Figure 26.: Comparison between the average spin current density $j_{\rm s}^{\rm av}$ flowing in the Ge layer (grey dashed line) and the one injected in a Pt layer grown on Ge (orange continuous line). In the latter case no sign inversion is expected within our model. Both spin current densities are normalized to the unity. Figure reproduced from Ref. [73].

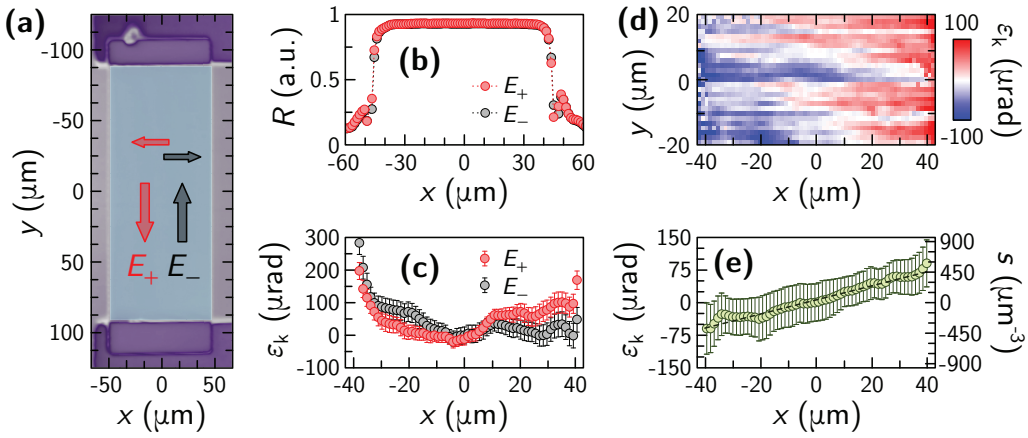

Figure 27.: (a) Optical reflectivity map of the sample for $\hbar\omega = 0.8$ eV. The Ge stripe, the Ni contacts and the Si substrate are depicted in light blue, violet and gray, respectively. The experimental data in panels (b,c) show the reflectivity and the ellipticity profiles, respectively, across the x-axis, for a positive (red dots) or negative (black dots) applied electric field along the y axis. All the data have been acquired with an absolute value of the electric field of 4.7 mV/μm. The profiles are obtained by averaging over the y-axis the data obtained in a scanned area of 130×40 μm^2. The dots represent the mean value, while the error bar shows twice the standard deviation of the data. A complete ellipticity map is shown in (d), obtained as the difference between the measurements with opposite electric fields. (e) Ellipticity ε_k and electrically-induced spin density s across the Ge channel. Figure adapted from Ref. [116].

By means of two ohmic contacts (Ni pads, 100 nm-thick), we apply an electric field $E_{+(-)}$ along the y axis. Due to SHE, the electric field generates at the edges of the Ge stripe (along the x axis) an accumulation of electrons with a spin polarization parallel to the out-of-plane direction (z axis), in agreement with eq. (31a). The applied electric field is less than 8 mV/μm, corresponding to a charge current density j lower than 8×10^3 A/cm^2. It is worth mentioning that the possibile magnetization of the Ni contacts is irrelevant for the injection of spin-polarized electrons in Ge due to the conductivity mismatch between Ni and Ge [23].

Since the direction of the spin polarization is perpedicular to the sample plane, we exploit the P-MOKE setup shown in Fig. 13 (a), with a balanced photodiode bridge acquisition, to simultaneously measure the Kerr ellipticity ε_k and the reflectivity of the sample (see Sec. **6**˙1). The light source is a 0.8 eV continuous-wave laser, with an optical power incident on the sample of 2 mW. Throughout all the measurements the sample is kept at $T = 20$ K. At this temperature, the Ge direct gap lies at $E_{\rm dg} \approx 0.86$ eV, as a result of both the effect of the temperature [154], and the band gap narrowing due to impurities [147]. It is worth noticing that the photon energy has been chosen to optimize the magnitude of the Kerr signal [155], and avoid optical absorption at Γ.

In Fig. 27 (b,c) we report the reflectivity [R, panel (b)] and the Kerr ellipticity [ε_k, panel (c)] measured for an applied electric field $E = 4.7$ mV/μm parallel (red circles) or anti-parallel (black circles) to the y axis. The profiles represent the spatial average along the y direction of 130×40 μm^2-wide maps. ε_k is reported only in a region between

$x \approx -40$ µm and $x \approx 40$ µm, to avoid possible optical artifacts related to the edges of the channel. As expected, the reflectivity profile does not change upon reversal of the applied current density, while ε_k shows a slope reversal for opposite directions of $\mathbf{j}$. Figure 27 (d) shows a complete ellipticity map of the scanned region, obtained as the difference between the Kerr ellipticity detected for E_+ and E_-. The averaging of the map reported in Fig. 27 (d) yields the Kerr ellipticity profile of Fig. 27 (e), also obtained as the difference of the two profiles shown in Fig. 27 (c). Since the measured Kerr ellipticity is proportional to the electrically-induced spin accumulation, the latter shows a linear dependence as a function of the x position.

As derived in Sec. **6**˙2, the electrically-induced spin density is expressed by eq. (31a), reported here for convenience:

$$s(x) = -\frac{\mu_\mathrm{t}}{D}\ell_\mathrm{s} n_0 \,\mathrm{sech}\left(\frac{d_x}{2\ell_\mathrm{s}}\right)\sinh\left(\frac{x}{\ell_\mathrm{s}}\right)E. \tag{36}$$

The dependence upon x is accounted only in the $\sinh(x/\ell_\mathrm{s})$ term, which can be approximated as $\sinh(x/\ell_\mathrm{s}) \approx x/\ell_\mathrm{s}$ for $x/\ell_\mathrm{s} \ll 1$. Since x ranges between $\pm d_x/2$, the approximation is valid for $\ell_\mathrm{s} \gg d_x/2$, as already pointed out in Fig. 14 (a). This nicely reproduces the observed linear profile of ε_k and suggests a long spin-diffusion length in heavily-doped Ge at low temperatures.

However, this does not allow estimating the value of ℓ_s directly from the experimental profiles of ε_k by means of eq. (36) (at variance with Ref. [48]), since any $\ell_\mathrm{s} > t/2$ would give a spin accumulation profile in agreement with the one experimentally observed. By exploiting the theoretical calculations of Sec. **4**, we can estimate a spin lifetime $\tau_\mathrm{s} = 420$ ns in Ge for $N_\mathrm{d} = 2.5 \times 10^{18}$ cm^{-3} at $T = 20$ K. To calculate the spin-diffusion length we infer from Hall measurements performed at the same temperature an electron mobility $\mu \approx 10^3$ cm^2 V^{-1}s^{-1}, in agreement with Ref. [156]. From the generalized Einstein equation [108] we obtain a diffusion coefficient $D = 23$ cm^2/s, which yields $\ell_\mathrm{s} \approx 31$ µm, a value compatible with the linear profile observed in Fig. 27 (e).

To perform a quantitative analysis of the spin-Hall effect in Ge, it is mandatory to find the relation between the electrically-induced spin accumulation and the measured Kerr ellipticity ε_k, which represents the responsivity of the experimental setup. To this purpose, optical orientation is employed to inject an electron population in the conduction band of Ge with a well-known spin polarization (pump beam). In this case we measure (probe beam) the Kerr ellipticity generated by the optically injected spins [see Fig. 28 (a)]. The direction of the pump beam is 45° with respect to the normal of the sample and the spot size is about 100 µm with 10 mW of optical power. The two beams have been focused and overlapped on the Ge surface. From Fig. 28 (b) it is straightforward to see that, by varying the DCP of the injected photons, we vary the injected spin polarization and eventually the detected ε_k value. The number of injected spins can be estimated by solving the standard spin drift-diffusion equation in the steady state conditions with an optical generation term [eq. (20)]. Since in our experimental case the absorption coefficient is $\alpha = 5$ cm^{-1} [157], while the stripe thickness is only $d_z = 3$ µm, we approximate the light absorption as constant over the whole stripe. This reduces eq. (20) to:

$$\frac{\partial^2 s}{\partial z^2} - \frac{s}{{\ell_\mathrm{s}}^2} = -\frac{P_{\mathrm{n},0}\Phi_\mathrm{ph}\alpha}{D} \tag{37}$$

and by imposing the boundary conditions $j_s(0, -d_z) = 0$ we obtain:

$$s = \tau_s \, P^z_{n,0} \Phi_{ph} \alpha, \tag{38}$$

being $P^z_{n,0}$ the electron spin polarization along the z axis. Since the pump beam illuminates the sample at 45° with respect to the normal, the polar angle in Ge is $\approx 10°$, meaning that the polarization vector is almost parallel to z, i.e., $P^z_{n,0} \approx P_{n,0}$. Since the incident photon energy is $\hbar\omega = 0.8$ eV, we can set $P_{n,0} = 50\%$ and therefore, from eq. (38) we can estimate a responsivity of the experimental setup $\eta = s/\varepsilon_k = 5.8$ µrad^{-1}µm^{-3}, which gives the spin density of Fig. 27 (e).

It is important to notice that at $T = 20$ K the direct gap of Ge lies at $E_{dg} \approx 0.86$ eV so that for $\hbar\omega = 0.8$ eV optical transitions are phonon mediated, only promoting spin-polarized electrons along the Λ direction of Ge. Since phonon-mediated optical transitions mostly preserve the spin polarization in the CB, at least for the case of Si (see Sec. **7**˙1.1), we can assume $P_{n,0} = 50\%$ also in Ge, being this case only an upper limit for the electron spin polarization. A lower value of $P_{n,0}$ would decrease η and consequently increase the estimated electrically-induced spin accumulation.

From the calibration procedure, we find $s \approx \pm 400$ µm^{-3} for $x \approx \pm 40$ µm when an electric field $E = 4.7$ mV/µm is applied [see Fig. 27 (e)]. This value is roughly two orders of magnitude larger than what measured in InGaAs [48] and comparable with GaAs [115], indicating a large spin accumulation in Ge bars.

In Fig. 29 we report the electric field dependence of the detected signal. The spin profiles are shown in panel (a) as a function of E between 0.4 mV/µm and 7.3 mV/µm. The spin density at the edges of the Ge channel increases as a consequence of the increase of E. In Fig. 29 (b) we evaluate the spin density at $x = 40$ µm by a linear fitting of the detected experimental profiles, which linearly increase with E as expected from eq. (36). In Fig. 29 (b) the spin current density flowing at the center ($x = 0$) of the Ge stripe is also reported, as calcuated from eq. (31b).

It is possible to estimate the transverse mobility $\mu_t = \gamma\mu$ and thus the spin-Hall angle γ as a function of the applied electric field. The results are reported in Fig. 30 (a). Since in

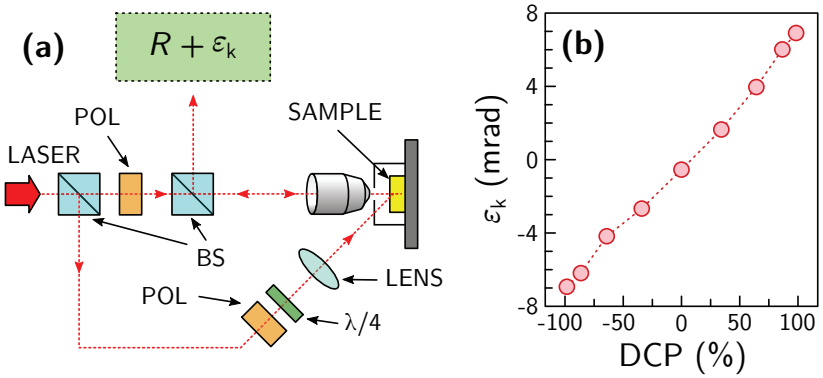

Figure 28.: (a) Setup for the calibration of MOKE in Ge: optical orientation is used to inject an electron population in Ge with a well-known spin polarizaiton and detect the resulting Kerr ellipticity as a function of the DCP. The experimental data are reported in (b). Figure adapted from Ref. [116].

our case the spin-diffusion length cannot be experimentally evaluated, in the calculations we exploit the theoretical value $\ell_s = 31$ µm. The average value of the spin-Hall angle is $\gamma = (1.9 \pm 0.2) \times 10^{-4}$, a value which nicely agrees with the one obtained at room temperature from spin-to-charge conversion measurements for thermalized electrons (see Sec. **7**˙3).

We have also investigated the temperature dependence of γ. In Fig. 30 (b) we report the measured spin accumulation at the edge of the scanned region, normalized to the applied electric field, as a function of the temperature. The spin density at $x = 40$ µm decreases as the temperature increases, following the temperature dependence of ℓ_s. We interpret the results within the same model presented before, which suggests a small temperature dependence of the spin-Hall angle.

7˙5. *SCI in Bi thin films grown on Ge(111).* – It has been demonstrated that a large Rashba effect occurs when a single layer of Bi is deposited on the top of a clean Ge(111) surface [158, 159]. In this frame, it appears particularly interesting to study the spin transport in the Bi/Ge(111) as a function of the Bi thickness in the ultrathin film limit, with Bi film thicknesses lower than 10 nm. In the following, we report on the thickness-dependent structural and electronic properties of Bi films and we present the results of SCI measurements. To investigate spin-charge conversion, we transfer spins to the Bi layer, either by means of optical orientation in the Ge substrate, or from ferromagnetic-resonance-driven (FMR) spin injection from an Al/Co/Al stack grown on the top of the Bi film. Moreover, charge-spin conversion measurements are performed by exploiting L-MOKE.

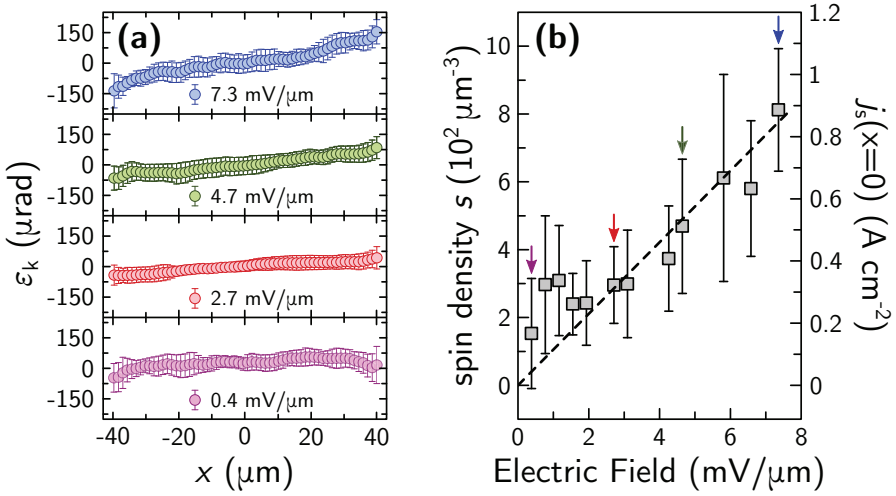

Figure 29.: (a) Kerr ellipticity profiles obtained for an applied electric field of 0.4 mV/µm (violet circles), 2.7 mV/µm (red circles), 4.7 mV/µm (green circles), and 7.3 mV/µm (blue circles). The error bars account for the standard deviation resulting from maps averaging over the y axis. (b) Spin density at the edge of the measured region and spin current density at the center (along x) of the Ge stripe. The data are extrapolated from a linear fitting of the profiles like the ones shown in panel (a). The colored arrows mark the data corresponding to the profiles shown in (a). Panel (b) is reproduced from Ref. [116].

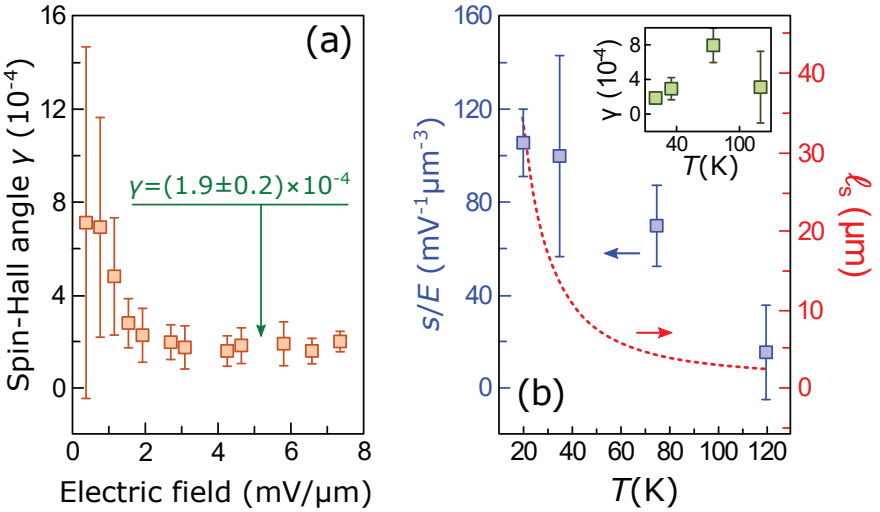

Figure 30.: (a) Spin-Hall angle γ as function of the electric field at $T = 20$ K. The average value, weighted by accounting for error bars, is $\gamma = (1.9 \pm 0.2) \times 10^{-4}$. (b) Temperature dependence of the electrically-induced spin density at the edges of the scanned area as a function of the temperature. The decrease of the signal (blue squares) follows the decrease of ℓ_s (red dotted line). The inset shows the γ value inferred from the temperature-dependent measurements. Figure reproduced from Ref. [116].

7˙5.1. *Structural and electronic properties*. The growth of thin Bi films on Ge(111) has been studied by means of scanning tunneling microscopy (STM), low-energy electron diffraction (LEED), reflection high-energy electron diffraction (RHEED), and X-ray diffraction. The results are discussed in details in Ref. [118]. The investigated samples have been grown *in situ* with molecular beam epitaxy, in UHV at room temperature. First, we grow a thin (1 ML-thick) Bi wetting layer on the top of Ge(111), which gives origin to the Bi/Ge($\sqrt{3}\times\sqrt{3}$) $R\,30°$ reconstruction, following a standard procedure in the literature [159, 158, 160]. Then, we deposit a variable Bi thickness t_{Bi}.

The results of the STM analysis are reported in Fig. 31. For $t_{\mathrm{Bi}} < 3.5$ nm the Bi atoms cluster in nanoislands [Fig. 31 (a)], of which the top facet shows the pseudocubic (PC) (110) phase [Fig. 32 (a,b)]. The lateral dimension a_{Bi} of the islands is of the order of tens of nanometers, as shown in Fig. 32 (d), increasing with the Bi thickness. Due to the presence of islands, the nominal thickness t_{Bi} of the film differs from the effective thickness h of the Bi nanocrystals [Fig. 32 (e)]. At $t_{\mathrm{Bi}} \approx 4$ nm the islands percolate, forming an almost continuous 2D layer [Fig. 31 (b)]. Also in this case the top facet still shows the PC phase. However, between 4 nm and 5 nm we observe the coexistence of the PC and the hexagonal (HEX) (111) phase. Finally, for $t_{\mathrm{Bi}} > 5$ nm the film undergoes to a structural change, since onlythe single crystalline HEX phase is observed [see Fig. 31 (c) and Fig. 32 (c)].

The investigation of the electronic properties of the system has been performed by means of spin- and angle-resolved photoemission spectroscopy (S-ARPES) on *in situ* grown samples. The measurements have been performed at the APE beamline of the Elettra synchrotron facility, with p-polarized synchrotron radiation at $\hbar\omega = 50$ eV, and an hemispherical electron momentum and energy analyzer (Scienta DA30). During the

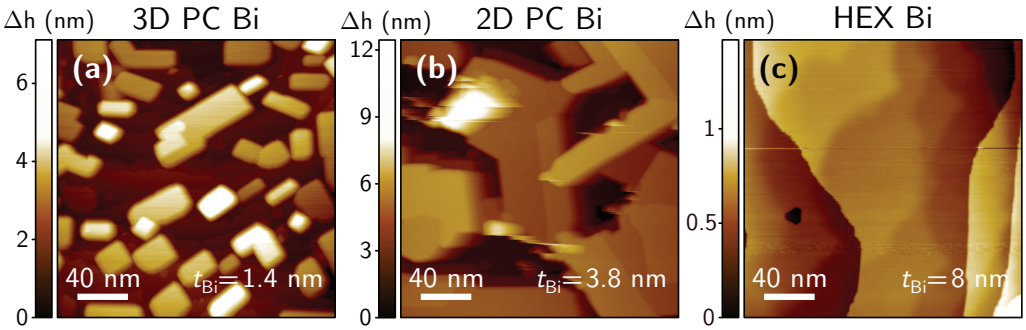

Figure 31.: Scanning tunneling microscopy images of Bi/Ge(111) at Bi thicknesses t_{Bi} of (a) 1.4 nm, (b) 3.8 nm, and (c) 8 nm, t_{Bi}. t_{Bi} is measured from the Bi/Ge wetting layer. Figure reproduced from Ref. [118].

measurements the sample was kept at $T = 77$ K. The experimental results are reported in Fig. 33 as a function of the Bi thickness. In the 3D-PC regime we observe states with a hole character, crossing the Fermi level around the $\overline{\Gamma}$ point [Fig. 33 (a-c)]. Notably, similar states have already been observed by Bian et al. [163] in the 2 nm-thick Bi/Si(111) heterostructure. In analogy with their observations, we conclude that these are surface states with a spatial extension of only 2 Bi bilayers (BL, being 1 BL = 3.28 Å). In this

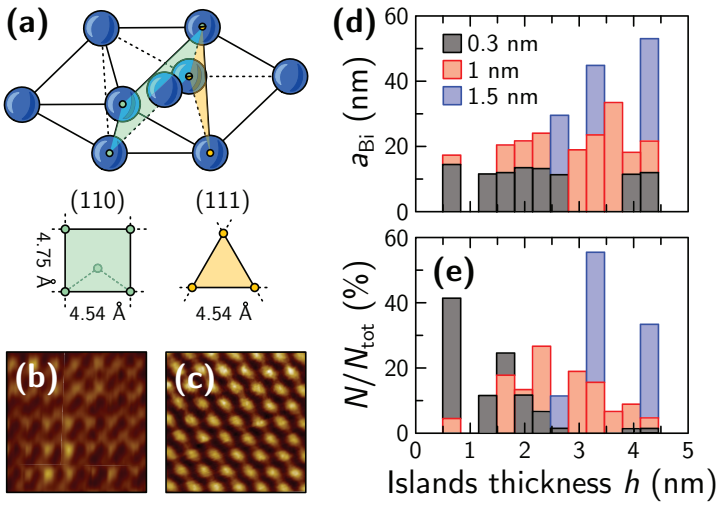

Figure 32.: (a) Bulk Bi unit cell, with the (110) pseudocubic (green) and (111) hexagonal (yellow) surfaces reported below. (b,c) 3×3 nm^2 STM images of Bi(110) and Bi(111) surfaces, taken at $t_{Bi} = 2.6$ nm and $t_{Bi} = 8$ nm, respectively. (d) Square root of the mean surface of the Bi islands in the 3D-PC regime as a function of the islands thickness h. (e) Fraction of the islands with a defined thickness h in the 3D-PC regime. The analysis has been carried out for $t_{Bi} = 0.3$ nm (black rectangles), $t_{Bi} = 1$ nm (red rectangles), and $t_{Bi} = 1.5$ nm (blue rectangles).

1008 regime we do not clearly observe other surface or bulk states close to E_F. For $t_{Bi} = 5$ nm

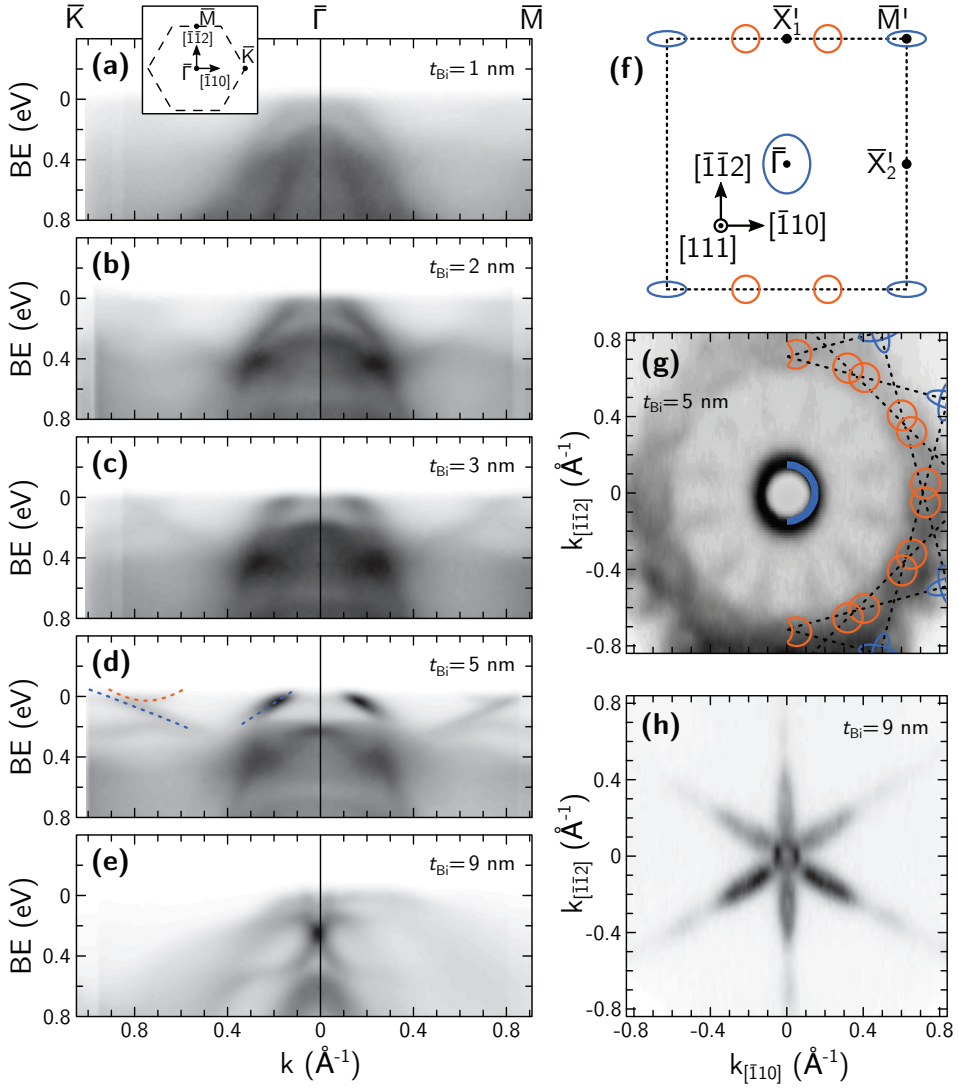

Figure 33.: (a-e) Angle-resolved photoemission spectroscopy measurements along the $\overline{K} - \overline{\Gamma} - \overline{M}$ direction of the Ge(111) surface Brillouin zone (SBZ), shown in the inset of panel (a), for $t_{Bi} = 1, 2, 3, 5$ and 9 nm. (f) Sketch of the Bi(110) Fermi surface (from Ref. [161]). $\overline{\Gamma}' = \overline{\Gamma}$, $\overline{M}'$, $\overline{X}_1$, and $\overline{X}_2'$ are the high symmetry points of the Bi(110) SBZ. (g) Experimental 2D Fermi surface for $t_{Bi} = 5$ nm, reproduced with the superposition of the sketch in (f), accounting for all the possible equivalent directions. (h) 2D Fermi surface for $t_{Bi} = 9$ nm, showing the typical sixfold symmetry associated with the single-crystalline HEX phase [162]. Orange and blue lines in (d,f,g) corresponds to electron and hole states, respectively. Figure reproduced from Ref. [118].

[Fig. 33 (d,g)] the band structure still shows states crossing the Fermi level around $\overline{\Gamma}$, but we clearly detect other states crossing the Fermi level at $|k| \approx 0.7$ Å^{-1} along both the $\overline{\Gamma} - \overline{K}$ and $\overline{\Gamma} - \overline{M}$ directions. In this case, it is worth comparing the experimental results with the expected Fermi contour for the (110) facet of the bulk Bi, reported in Fig. 33 (f). Twofold PC Bi can grow on six equivalent orientation on the sixfold (111) surface of Ge, as already observed by Hatta et al. [164] with LEED analysis. Therefore, the multiplicity of the configurations explains also the analogies between the ARPES data acquired along the $\overline{\Gamma} - \overline{K}$ and $\overline{\Gamma} - \overline{M}$ directions. Thus, the states crossing E_F for $|k| > 0.8$ Å^{-1} [blue dotted line in Fig. 33 (d)] are given by the ring states around the $\overline{M}'$ point of Bi(110) SBZ [Fig. 33 (f)]. The states, symmetric with respect to $|k| \approx 0.7$ Å^{-1} [orange dotted line in Fig. 33 (d)], are marked by orange circles along the $\overline{X}'_1 - \overline{M}'$ direction [Fig. 33 (f)] of other two equivalent Bi cells. In Fig. 33 (e,h) the band structure along the $\overline{\Gamma} - \overline{K}$ and $\overline{\Gamma} - \overline{M}$ directions of the Ge(111) SBZ is reported together with the Fermi surface, for $t_{Bi} = 9$ nm. In this regime we detect only the crystalline HEX phase of Bi in registry with the Ge(111) substrate.

Under the same conditions, we probe the in-plane components of the spin polarization by means of a very-low-energy electron diffraction (V-LEED) detector [165, 166]. The results of the S-ARPES measurements are reported in Fig. 34. In panels (a-d) we measure the spin polarization of the surface states observed with ARPES around the $\overline{\Gamma}$ point for $t_{Bi} = 2.5$ nm. The latters clearly show a net spin polarization at the Fermi level which reaches up to 40%. The direction of the spin polarization is fully determined by the direction of the momentum, i.e., suggesting the presence of spin-momentum locking (SML), with a counterclockwise helical spin texture. It is interesting to notice that also the states from $\overline{M}'$ are spin polarized with $P_n \approx 33\%$ (Fig. 34 (e-g)). However, at variance with the states around $\overline{\Gamma}$, their spin texture is clockwise, as already indicated in Ref. [167].

7˙5.2. *SCI measurements.* Charge-to-spin conversion measurements have been performed by applying a voltage difference to a a macroscopic Bi/Ge(111) 1.5×5 mm^2 stripe of constant Bi thickness t_{Bi}. The conversion of the charge current into a spin current and, consequently, the generation of an electrically-induced spin accumulation is generated via REE (see Sec. **2**˙2). Since the measurements have been performed in air and at room temperature, the samples are capped with a ZrO_2(10 nm)/MgO(5 nm) bilayer to prevent the oxidation of the Bi layer and the oxide bilayer is optically inactive in the explored wavelength range. We perform L-MOKE to probe the in-plane spin accumulation by means of the experimental setup reported in Fig. 13 (b). In this case, the incoming s-polarized light beam ($\lambda = 691$ nm) is focused on the sample with a polar angle $\vartheta = 45°$, and the signal proportional to the Kerr ellipticity ε_k is recorded by means of a photodiode. The resulting ε_k is reported in Fig. 35 as a function of the Bi thickness. It is straightforward to see that a large Kerr signal is detected up to $t_{Bi} = 3$ nm (orange band in Fig. 35), whereas the signal rapidly decreases as the thickness is increased.

We also investigate the spin-charge conversion given by IREE in Bi. In this case, spins are generated either by exploiting the optical orientation in Ge (as previously discussed for Pt/semiconductors in Sec. **7**˙1), or with FMR-driven spin injection. Once again, the Bi film has been coated with a ZrO_2(10 nm)/MgO(5 nm) bilayer, while an Al(5 nm)/Co(10 nm)/Al(5 nm) stack was grown on the top of the Bi film in order to perform FMR spin injection. For optical orientation we exploit a 740 nm laser source and we measure the photoinduced IREE by acquiring the voltage between two ohmic contacts

deposited on the top of Bi. The charge current I is obtained from the ratio between the measured voltage difference ΔV under open circuit conditions and the electrical resistance R of the conductive path, estimated in a four-probe configuration. The experimental results, normalized to the photon flux $\Phi_{\rm ph}$, are reported in Fig. 36 (a). It is worth mentioning that the trend of this spin-charge conversion is similar to the one shown in Fig. 35.

In the case of FMR driven spin injection, a transverse radio frequency field $H_{\rm rf}$ triggers the FMR of the Co layer, and thus the spin pumping into Bi. In Fig. 36 (b) we report the

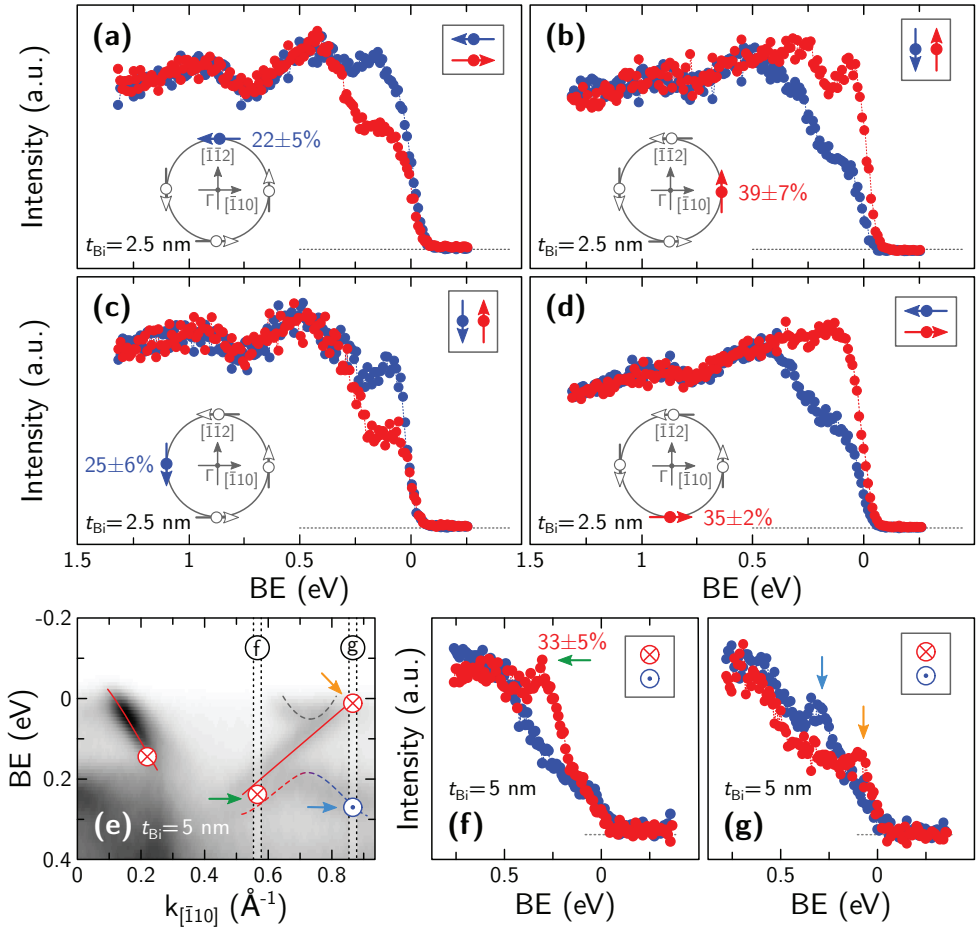

Figure 34.: (a-d) Spin-resolved ARPES around the Γ point for $t_{\rm Bi} = 2.5$ nm. The percentage values correspond to the net spin polarization at the Fermi level. (e) Band structure along the $\overline{\Gamma} - \overline{K}$ direction, for $t_{\rm Bi} = 5$ nm, as shown in Fig. 33 (d). The red solid lines show the hole states of Bi(110) around $\overline{\Gamma}$ (left line) and $\overline{M}'$ (right line). The dashed lines show the electrons states related to different equivalent Bi cells. The line colors and the inward/outward vector symbols show the direction of the spin polarization. (f,g) S-ARPES around $\overline{M}'$ for the momentum position reported in panel (e). Figure reproduced from Ref. [118].

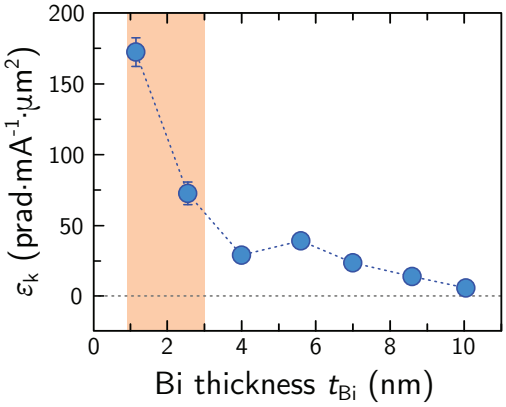

Figure 35.: Kerr ellipticity ε_k as a function of the Bi thickness t_{Bi}, induced by the Rashba-Edelstein effect in the Bi film. Each data point represents the mean value of ten acquisitions with an integration time of 500 s, while the error bars accounts for the fluctuations of the signal, showing twice the standard deviation of the measurements. Figure reproduced from Ref. [118].

charge current $I = \Delta V/R$, normalized to the excitation signal, i.e., the radiofrequency power, proportional to ${H_{\mathrm{rf}}}^2$. The experimental results of Fig. 36 (a) and 36 (b) clearly show the same qualitative behavior: a large signal is measured for a small Bi thickness, whereas the signal completely disappears within the experimental error for $t_{\mathrm{Bi}} > 4$ nm. Notably, at $T = 30$ K the FMR-driven IREE signal is roughly one order of magnitude larger compared to what obtained at room temperature.

7˙5.3. *Discussion.* S-ARPES experimental results indicate the presence of spin-polarized surface states at the Fermi level, where SCI can occur, thanks to SML. However, from simple symmetry arguments it is possible to argue that the chirality of the SML should be opposite at the top and bottom surface of the Bi layer. This results from the inversion of the direction of the spin-polarization without inversion of the momentum upon mirror symmetry, as pictorially sketched in Fig. 37. Evidently, an opposite chirality of SML in the surface states yields opposite SCI contributions. As a consequence, when both the Bi interfaces are involved in SCI, the overall signal cancels out. Therefore, to preserve a net SCI signal, the two surfaces should be disentangled.

STM analysis suggests that the SCI signal is present in the Bi thickness range corresponding to the presence of Bi nanoislands, whereas it decreases as the clusters start to percolate. Since the lateral size a_{Bi} of Bi nanocrystals [Fig. 32 (d)] is comparable with the Fermi wavelength λ_{F} in Bi (between 40 and 70 nm [168, 169]), while the height of the nanocrystals is much smaller than a_{Bi}, quantum confinement can play a fundamental role in the transport properties of the system. The appearance of *quantum size effects* (QSE) in Bi is further favored by the small electron effective mass, between 10^{-3} m_0 and 0.26 m_0, depending on the crystalline orientation [170]. Indeed, the presence of QSE in Bi has been already reported in the literature [162, 171]. Moreover, Bi is a semimetal, the lowest electron band being at the L point, and the highest hole band at the T point. The gap between the states at the L point is $E_{gL} = 15$ meV, while $E_{\mathrm{ig}} = -38$ meV is the indirect band overlap between the states at L and T points [172, 162], as shown in

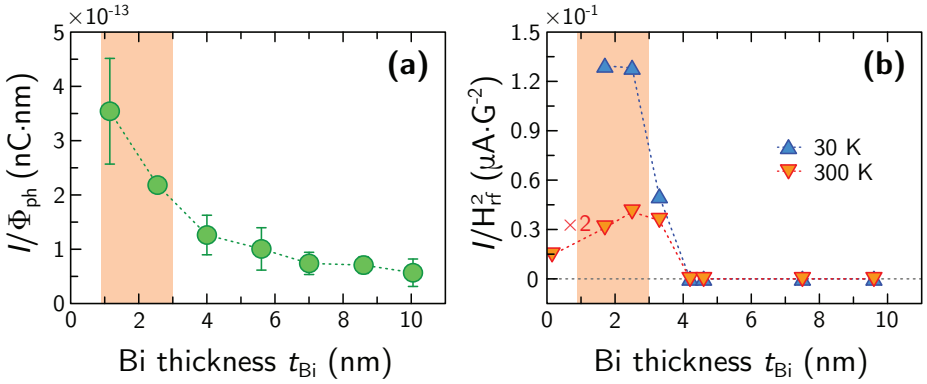

Figure 36.: (a) Optically-induced IREE signal, normalized to the photon flux $\Phi_{\rm ph}$, for Bi/Ge(111) as a function of the Bi thickness. I is the charge current obtained as $\Delta V/R$, being ΔV the measured voltage difference and R the electrical resistance of the conductive path. (b) FMR-driven IREE signal, normalized to the radio frequency power, at $T = 30$ K (blue upwards triangles) and $T = 300$ K (red downwards triangles). Figure reproduced from Ref. [118].

Fig. 38 (a). The QSE can separate the discrete energy levels enough to open a bandgap $E'_{\rm g}$ in Bi nanocrystals [172],thus inducing a *semimetal-to-semiconductor transition* (SMSC).

The bandgap opening can be interpreted within the model of Ref. [172], which predicts a SMSC transition (i.e., $E'_{\rm g} \geq 0$) for $a_{\rm Bi} \leq 50$ nm, [see Fig. 38 (b)]. Thus, nanocrystals of lateral size $a_{\rm Bi} \leq 50$ nm and thicker than 4 BL (the latter condition meaning that opposite surface states do not overlap each other [163]) are expected to be semiconducting.

The fraction δ of the surface which fulfill these conditions is reported in Fig. 39, as extrapolated from the STM analysis. For $t_{\rm Bi} < 0.9$ nm, most of the nanocrystals are less than 4 BL-thick, while for $t_{\rm Bi} > 3$ nm only a small fraction of the nanocrystals is small enough to give the SMSC transition. The thickness range between 0.9 and 3 nm is the one where most of the nanocrystals can show a bulk gap. Evidently, the direct contact between Bi and Ge on one side and on MgO or Al on the other side could however affect the electronic properties of the Bi layer, e.g., the band structure, confining potentials, and effective masses. Thus, the calculated $E'_{\rm g}$ is an upper bound estimation, while, more realistically, the QSE triggers a decrease of the density of states at the Fermi level, producing an increase of the bulk resistance for the nanocrystals which fulfill the criteria for $E'_{\rm g} > 0$.

Therefore, in our experiments, for (0.9 nm $< t_{\rm Bi} <$ 3 nm) SCI mainly occurs at the interface where the spin is injected (Bi/Ge for optical orientation and Bi/Al for FMR-driven spin injection), thus providing a net SCI signal. This thickness range is reported as an orange band in Figs. 35 (b) and 36. Indeed a large Kerr signal, proportional to the electrically-induced spin density at the Bi/Ge interface, is detected for 0.9 nm $< t_{\rm Bi} <$ 3 nm, since the presence of nanoislands with a high bulk resistance prevents most of the applied current from flowing at at the top Bi surface (Fig. 35). Thus, REE at the Bi/Ge interface generates an in-plane spin accumulation with a spin polarization perpendicular to the current density vector. For $t_{\rm Bi} > 3$ nm, nanocrystals start percolating and exhibit lateral sizes larger than $\lambda_{\rm F}$. This diminishes quantum confinement, allowing the spin-polarized electrons to diffuse in the entire film thickness. Since $h < \ell_{\rm s}$,

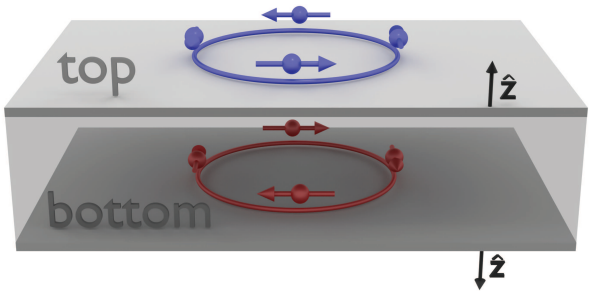

Figure 37.: Sketch of the chirality of the states with spin-momentum locking at the Bi surfaces.

spin-to-charge conversions at opposite interfaces compensate each other, drastically reducing the overall signal. Similarly, for charge-to-spin conversion, when nanocrystals become gradually conducting in the bulk, the electrical current flows at both interfaces, causing opposite spin accumulations, which tend to cancel each other, decreasing the Kerr signal. We can model the effect of quantum confinement within a simple picture, in which a variable bulk resistance R_{B} electrically connects the top and bottom metallic surface states of resistance R_{S}. When confinement leads to $R_{\mathrm{B}} \gg R_{\mathrm{S}}$, the surface states are electrically disentangled ($0.9\ \mathrm{nm} < t_{\mathrm{Bi}} < 3\ \mathrm{nm}$), while for $t_{\mathrm{Bi}} > 3$ nm, $R_{\mathrm{B}} \approx R_{\mathrm{S}}$ and the charge currents in the top and bottom surface states are shunted through the bulk, reducing and then cancelling SCI signals. It is also worth to remind that from $t_{\mathrm{Bi}} = 3$ nm, $\overline{M}'$ surface states at E_{F} develop at the surface of Bi nanocrystals and of films as shown in Fig. 33. They exhibit a hole character and a spin chirality opposite to the one of $\overline{\Gamma}$ states (Fig. 34) and thus contribute to the decrease of conversion signals.

From the spin-to-charge measurements, we can give an estimation of the 2D-SCI

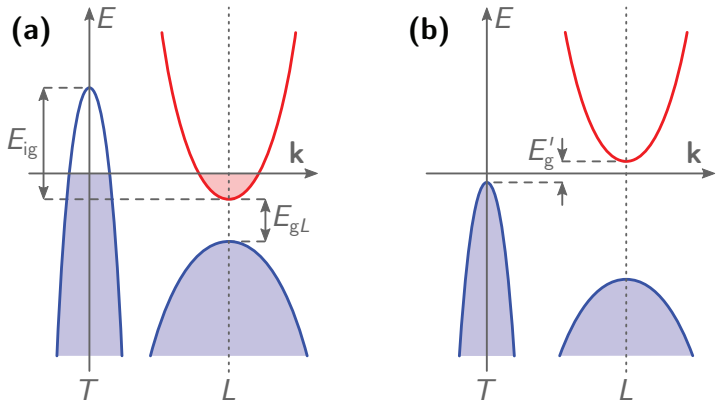

Figure 38.: Hole (blue) and electron (red) pockets at the L and T point of bulk Bi without (a), and with (b) the effect of quantum confinement. Without confinement an indirect overlap $E_{\mathrm{ig}} = -38$ meV is present between the states at L and T, whereas $E_{gL} = 15$ meV is the bandgap at L. In presence of quantum confinement an indirect bandgap E_{ig} can be opened.

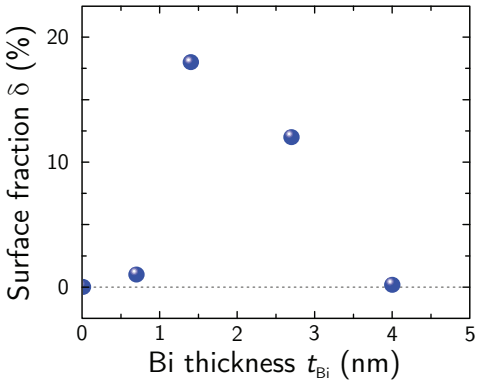

Figure 39.: Fraction of the Bi surface, as a function of the Bi thickness, which fulfills the conditions for SMSC transition: $a_{\mathrm{Bi}} \leq 50$ nm, and $h < 4$ BL. Figure reproduced from Ref. [118].

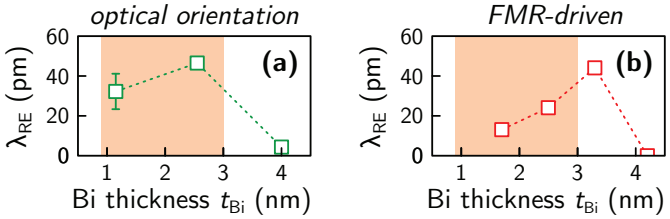

Figure 40.: Rashba-Edelstein length estimated from optical (a) and FMR driven (b) spin injection. Figure reproduced from Ref. [118].

efficiency, i.e., the Rashba-Edelstein length λ_{RE} [eq. (6)]. By assuming that the fraction of the sample which is active for SCI is the sample surface δ covered with semiconducting nanocrystals, as shown in Fig. 39, we can evaluate the spin current density injected into the Bi surface by means of the Spicer-like model [eq. (23)] and estimate λ_{RE}, as shown in Fig. 40. We obtain a maximum value of $\lambda_{\mathrm{RE}} \approx 50$ pm for both optical spin orientation and spin pumping for $t_{\mathrm{Bi}} \approx 3$ nm. The calculation suggests that the SCI efficiency is comparable at the Bi/Ge and Bi/Al interfaces. It is important to note that the calculation of λ_{RE} is performed under the assumption that the bulk resistance of the nanocrystals is large enough to completely avoid the coupling between interfaces, so that $\lambda_{\mathrm{RE}} = 50$ pm represents a lower bound estimation of the SCI efficiency. The value is comparable with the ones obtained when the Bi is grown on different materials, such as Ag ($1 - 300$ pm) [49, 173, 174], Cu (9 pm) [175], or with the case of the Ag/Sb Rashba interface (30 pm) [173]. From eq. (6) the Rashba-Edelstein length can be expressed as $\lambda_{\mathrm{RE}} = \alpha_{\mathrm{R}}\tau_{\mathrm{m}}/\hbar$ where α_{R} is the Rashba coefficient and τ_{m} is the momentum relaxation time in the interface states. Exploiting the results from Ref. [176], we estimate $\alpha_{\mathrm{R}} \approx 1.5$ eV $\cdot$ Å at the Bi(110) surface. This produces $\tau_{\mathrm{m}} \approx 0.2$ fs, which is of the same order of magnitude of what obtained in other Rashba systems [49, 177, 175].

8. – Summary

In this paper, we have reviewed the main experimental results concerning the spin-charge interconversion phenomena in group-IV semiconductors, with particular attention to germanium. It has been demonstrated that Ge is a suitable platfrom to implement non-local architectures, where spin is optically injected and electrically detected, without the use of any ferromagnet. In this respect, spin diffusion lengths in low-n-doped Ge at room temperature of about 10 µm have been measured, a value much larger than the common sizes of the electronic devices. Moreover, Ge provides for interesting spin-charge interconversion properties, which can be exploited both in the bulk of the material and at the surface, where spin-polarized surface states can be detected if thin Bi films are deposited on top of Ge. Therefore, all these features make Ge a natural candidate as a hosting material for the design and the engineering of spin-based devices.

* * *

The authors acknowledge A. Picone, A. Calloni, G. Bussetti, A. Brambilla, L. Duò, L. Ghirardini, M. Celebrano, A. Ferrari, S. Dal Conte, J. Frigerio, E. Carpene, G. Cerullo, C. Vergnaud, and M. Jamet.

REFERENCES

[1] Žutić I., Fabian J. and Das Sarma S., *Reviews of Modern Physics*, **76** (2004) 323. URL https://link.aps.org/doi/10.1103/RevModPhys.76.323

[2] Baibich M. N., Broto J. M., Fert A., Van Dau F. N., Petroff F., Etienne P., Creuzet G., Friederich A. and Chazelas J., *Physical Review Letters*, **61** (1988) 2472. URL https://link.aps.org/doi/10.1103/PhysRevLett.61.2472

[3] Fert A., *Reviews of Modern Physics*, **80** (2008) 1517. URL https://link.aps.org/doi/10.1103/RevModPhys.80.1517

[4] Julliere M., *Physics Letters A*, **54** (1975) 225 . URL http://www.sciencedirect.com/science/article/pii/0375960175901747

[5] Butler W. H., Zhang X.-G., Schulthess T. C. and MacLaren J. M., *Physical Review B*, **63** (2001) 054416. URL https://link.aps.org/doi/10.1103/PhysRevB.63.054416

[6] Mathon J. and Umerski A., *Physical Review B*, **63** (2001) 220403. URL https://link.aps.org/doi/10.1103/PhysRevB.63.220403

[7] Berger L., *Physical Review B*, **54** (1996) 9353. URL https://link.aps.org/doi/10.1103/PhysRevB.54.9353

[8] Slonczewski J., *Journal of Magnetism and Magnetic Materials*, **159** (1996) L1 . URL http://www.sciencedirect.com/science/article/pii/0304885396000625

[9] Myers E. B., Ralph D. C., Katine J. A., Louie R. N. and Buhrman R. A., *Science*, **285** (1999) 867. URL http://science.sciencemag.org/content/285/5429/867

[10] Chappert C., Fert A. and Nguyen Van Dau F., *Nature Materials*, **6** (2007) 813.

[11] Dyakonov M. and Perel V., *JETP Letters*, **13** (1971) 467 .

[12] Dyakonov M. and Perel V., *Physics Letters A*, **35** (1971) 459 . URL http://www.sciencedirect.com/science/article/pii/0375960171901964

[13] Edelstein V., *Solid State Communications*, **73** (1990) 233. URL http://linkinghub.elsevier.com/retrieve/pii/003810989090963C

[14] Miron I. M., Gaudin G., Auffret S., Rodmacq B., Schuhl A., Pizzini S., Vogel J. and Gambardella P., *Nature Materials*, **9** (2010) 230.

[15] Miron I. M., Garello K., Gaudin G., Zermatten P.-J., Costache M. V., Auffret S., Bandiera S., Rodmacq B., Schuhl A. and Gambardella P., *Nature*, **476** (2011) 189.

[16] Prenat G., Jabeur K., Vanhauwaert P., Pendina G. D., Oboril F., Bishnoi R., Ebrahimi M., Lamard N., Boulle O., Garello K., Langer J., Ocker B., Cyrille M., Gambardella P., Tahoori M. and Gaudin G., *IEEE Transactions on Multi-Scale Computing Systems*, **2** (2016) 49.

[17] Manchon A., Koo H. C., Nitta J., Frolov S. M. and Duine R. A., *Nature Materials*, **14** (2015) 871.

[18] Ohno H., Shen A., Matsukura F., Oiwa A., Endo A., Katsumoto S. and Iye Y., *Applied Physics Letters*, **69** (1996) 363.
URL https://doi.org/10.1063/1.118061

[19] Ohno H., *Science*, **281** (1998) 951.
URL http://science.sciencemag.org/content/281/5379/951

[20] Dietl T., Ohno H., Matsukura F., Cibert J. and Ferrand D., *Science*, **287** (2000) 1019.
URL http://science.sciencemag.org/content/287/5455/1019

[21] Xia J., Ge W. and Chang K., *Semiconductor Spintronics* (World Scientific Publishing) 2012.

[22] Chen L., Yang X., Yang F., Zhao J., Misuraca J., Xiong P. and von Molnï¿½r S., *Nano Letters*, **11** (2011) 2584.

[23] Fert A. and Jaffrès H., *Physical Review B*, **64** (2001) 184420.
URL https://link.aps.org/doi/10.1103/PhysRevB.64.184420

[24] Smith D. L. and Silver R. N., *Physical Review B*, **64** (2001) 045323.
URL https://link.aps.org/doi/10.1103/PhysRevB.64.045323

[25] Lampel G., *Physical Review Letters*, **20** (1968) 491.
URL https://link.aps.org/doi/10.1103/PhysRevLett.20.491

[26] Pierce D. T. and Meier F., *Physical Review B*, **13** (1976) 5484.

[27] Meier F. and Zakharchenya B. P., *Optical Orientation* (Elsevier) 1984.

[28] Takahashi R., Matsuo M., Ono M., Harii K., Chudo H., Okayasu S., Ieda J., Takahashi S., Maekawa S. and Saitoh E., *Nature Physics*, **12** (2015) 52.

[29] Žutić I. and Matos-Abiague A., *Nature Physics*, **12** (2015) 24.

[30] Fabian J., Matos-Abiague A., Ertler C., Stano P. and Žutić I., *Acta Physica Slovaca. Reviews and Tutorials*, **57** (2007) .
URL http://www.degruyter.com/view/j/apsrt.2007.57.issue-4-5/v10155-010-0086-8/v10155-010-0086-8.xm

[31] Li P., Song Y. and Dery H., *Physical Review B*, **86** (2012) 085202.
URL http://link.aps.org/doi/10.1103/PhysRevB.86.085202

[32] Zucchetti C., Bottegoni F., Vergnaud C., Ciccacci F., Isella G., Ghirardini L., Celebrano M., Rortais F., Ferrari A., Marty A., Finazzi M. and Jamet M., *Physical Review B*, **96** (2017) 014403.
URL http://link.aps.org/doi/10.1103/PhysRevB.96.014403

[33] Hamaya K., Fujita Y., Yamada M., Kawano M., Yamada S. and Sawano K., *Journal of Physics D: Applied Physics*, **51** (2018) 393001.
URL http://stacks.iop.org/0022-3727/51/i=39/a=393001

[34] Aruga T., *Journal of Electron Spectroscopy and Related Phenomena*, **201** (2015) 74 , special issue on electron spectroscopy for Rashba spin-orbit interaction.
URL http://www.sciencedirect.com/science/article/pii/S0368204814002254

[35] Datta S. and Das B., *Applied Physics Letters*, **56** (1990) 665.
URL https://doi.org/10.1063/1.102730

[36] Hall K. C., Lau W. H., Gï¿½ndogdu K., Flattï¿½ M. E. and Boggess T. F., *Applied Physics Letters*, **83** (2003) 2937.
URL https://doi.org/10.1063/1.1609656

[37] Xu Y., Awschalom D. D. and Nitta J., *Handbook of Spintronics* (Springer Netherlands) 2016.

[38] Chuang P., Ho S.-C., Smith L. W., Sfigakis F., Pepper M., Chen C.-H., Fan J.-C., Griffiths J. P., Farrer I., Beere H. E., Jones G. A. C., Ritchie D. A. and T.-M. C., *Nature Nanotechnology*, **10** (2015) 35.

[39] Choi W. Y., Kim H.-J., Chang J., Han S. H., Abbout A., Saidaoui H. B. M., Manchon A., Lee K.-J. and Koo H. C., *Nano Letters*, **18** (2018) 7998.
URL https://doi.org/10.1021/acs.nanolett.8b03998

[40] Wunderlich J., Park B.-G., Irvine A. C., Zârbo L. P., Rozkotová E., Nemec P., Novák V., Sinova J. and Jungwirth T., *Science*, **330** (2010) 1801.
URL http://science.sciencemag.org/content/330/6012/1801

[41] Betthausen C., Dollinger T., Saarikoski H., Kolkovsky V., Karczewski G., Wojtowicz T., Richter K. and Weiss D., *Science*, **337** (2012) 324.
URL http://science.sciencemag.org/content/337/6092/324

[42] Hochberg M. and Baehr-Jones T., *Nature Photonics*, **4** (2010) 492.
URL http://dx.doi.org/10.1038/nphoton.2010.172 http://www.nature.com/doifinder/10.1038/nphoton.2010.172

[43] Schï¿½ffler F., *Semiconductor Science and Technology*, **12** (1997) 1515.
URL http://stacks.iop.org/0268-1242/12/i=12/a=001

[44] Isella G., Chrastina D., Rï¿½ssner B., Hackbarth T., Herzog H.-J., Kï¿½nig U. and von Kï¿½nel H., *Solid-State Electronics*, **48** (2004) 1317, strained-Si Heterostructures and Devices.
URL http://www.sciencedirect.com/science/article/pii/S0038110104000565

[45] Süess M. J., Geiger R., Minamisawa R. a., Schiefler G., Frigerio J., Chrastina D., Isella G., Spolenak R., Faist J. and Sigg H., *Nature Photonics*, **7** (2013) 466.
URL http://john.mer.utexas.edu/A235FB325D345AC9F0E/FTP/papers/JohnPaperPresentations/July 16/nphoton.2013.67.pdf http://www.nature.com/doifinder/10.1038/nphoton.2013.67

[46] Hirsch J., *Physical Review Letters*, **83** (1999) 1834.
URL http://link.aps.org/doi/10.1103/PhysRevLett.83.1834

[47] Zhang S., *Physical Review Letters*, **85** (2000) 393.
URL https://link.aps.org/doi/10.1103/PhysRevLett.85.393

[48] Kato Y. K., Myers R. C., Gossard A. C. and Awschalom D. D., *Science*, **306** (2004) 1910.
URL http://www.sciencemag.org/cgi/doi/10.1126/science.1152697 http://www.sciencemag.org/cgi/doi/10.1126/science.1105514

[49] Rojas-Sánchez J. C., Vila L., Desfonds G., Gambarelli S., Attané J. P., De Teresa J. M., Magén C. and Fert A., *Nature Communications*, **4** (2013) 2944.
URL http://www.ncbi.nlm.nih.gov/pubmed/24343336%5Cnhttp://www.nature.com/doifinder/10.1038/ncomms3 http://www.nature.com/doifinder/10.1038/ncomms3944

[50] Dyakonov M., *Spin Physics in Semiconductors* (Springer) 2008.

[51] Bakun A. A., Zakharchenya B. P., Rogachev A. A., Tkachuk M. N. and Fleisher V. G., *JETP Letters*, **40** (1984) 1293 .

[52] Smit J., *Physica*, **24** (1958) 39 .
URL http://www.sciencedirect.com/science/article/pii/S0031891458935419

[53] Berger L., *Physical Review B*, **2** (1970) 4559.
URL https://link.aps.org/doi/10.1103/PhysRevB.2.4559

[54] Nozières P. and Lewiner C., *Journal de Physique*, **34** (1973) 901.

[55] Rashba E. I., *Semiconductors*, **42** (2008) 905.
URL https://doi.org/10.1134/S1063782608080046

[56] Sinova J., Valenzuela S. O., Wunderlich J., Back C. and Jungwirth T., *Reviews of Modern Physics*, **87** (2015) 1213.
URL http://link.aps.org/doi/10.1103/RevModPhys.87.1213

[57] Guo G., Murakami S., Chen T.-W. and Nagaosa N., *Physical Review Letters*, **100** (2008) 096401.
URL https://journals.aps.org/prl/abstract/10.1103/PhysRevLett.100.096401

[58] Bychkov Y. A. and Rashba E. I., *JETP Letters*, **39** (1984) .
URL http://stacks.iop.org/0022-3727/48/i=6/a=065001?key=crossref.a8a13589ae139b5a325a8482a80354bd

[59] Hasan M. Z. and Kane C. L., *Reviews of Modern Physics*, **82** (2010) 3045.
URL https://link.aps.org/doi/10.1103/RevModPhys.82.3045

[60] Rojas-Sánchez J.-C., Oyarzún S., Fu Y., Marty A., Vergnaud C., Gambarelli S., Vila L., Jamet M., Ohtsubo Y., Taleb-Ibrahimi A., Le Fèvre P., Bertran F., Reyren N., George J.-M. and Fert A., *Physical Review Letters*, **116** (2016) 096602.
URL https://link.aps.org/doi/10.1103/PhysRevLett.116.096602

[61] Gambardella P. and Miron I. M., *Philosophical Transactions of the Royal Society of London A: Mathematical, Physical and Engineering Sciences*, **369** (2011) 3175.
URL http://rsta.royalsocietypublishing.org/content/369/1948/3175

[62] Gorini C., Sheikhabadi A. M., Shen K., Tokatly I. V., Vignale G. and Raimondi R., *Physical Review B*, **95** (2017) 205424.
URL https://journals.aps.org/prb/abstract/10.1103/PhysRevB.95.205424

[63] Luengo-Kovac M., Huang S., Del Gaudio D., Occena J., Goldman R. S., Raimondi R. and Sih1 V., *Physical Review B*, **96** (2017) 195206.
URL https://journals.aps.org/prb/abstract/10.1103/PhysRevB.95.205424

[64] Parsons R., *Physical Review Letters*, **23** (1969) 1152.
URL http://link.aps.org/doi/10.1103/PhysRevLett.23.1152

[65] Ekimov A. I. and Safarov V. I., *ZhETF Pis. Red.*, **12** (1970) 293.

[66] Tinkham M., *Group Theory and Quantum Mechanics* (Dover Publications) 1964.

[67] Bassani F. and Pastori Parravicini G., *Electron states and optical transitions in solids* (Pergamon Press Ltd.) 1975.

[68] Beth R. A., *Physical Review*, **50** (1936) 115.
URL https://link.aps.org/doi/10.1103/PhysRev.50.115

[69] Rioux J. and Sipe J. E., *Physical Review B*, **81** (2010) 155215.
URL https://link.aps.org/doi/10.1103/PhysRevB.81.155215

[70] Dresselhaus G. and Dresselhaus M. S., *Solid State Physics: The Optical Properties of Solids* (Academic New York) 1966.

[71] Cheng J. L., Rioux J., Fabian J. and Sipe J. E., *Physical Review B*, **83** (2011) 165211.
URL https://link.aps.org/doi/10.1103/PhysRevB.83.165211

[72] Bottegoni F., Zucchetti C., Ciccacci F., Finazzi M. and Isella G., *Applied Physics Letters*, **110** (2017) 042403.
URL https://doi.org/10.1063/1.4974820

[73] Zucchetti C., Bottegoni F., Isella G., Finazzi M., Rortais F., Vergnaud C., Widiez J., Jamet M. and Ciccacci F., *Physical Review B*, **97** (2018) 125203.
URL https://doi.org/10.1103/PhysRevB.97.125203
https://link.aps.org/doi/10.1103/PhysRevB.97.125203

[74] Elliott R. J., *Physical Review*, **96** (1954) 266.
URL https://link.aps.org/doi/10.1103/PhysRev.96.266

[75] Yafet Y., *Solid State Physics*, **14** (1963) 1 .
URL http://www.sciencedirect.com/science/article/pii/S0081194708602593

[76] Pikus G. E. and Titkov A. N., *Spin relaxation under optical orientation in semiconductors*, in *Optical Orientation*, edited by Meier F. and Zakharchenya B. P., Vol. 8 of *Modern Problems in Condensed Matter Sciences* (Elsevier) 1984, pp. 73 – 131.
URL http://www.sciencedirect.com/science/article/pii/B9780444867414500081

[77] Yu T. and Wu M. W., *Journal of Physics: Condensed Matter*, **27** (2015) 255001.
URL http://iopscience.iop.org/0953-8984/27/25/255001
http://stacks.iop.org/0953-8984/27/i=25/a=255001?key=crossref.b935ba45bcfa09cd078077ef447b2b99

[78] Guite C. and Venkataraman V., *Applied Physics Letters*, **101** (2012) 252404.
URL http://aip.scitation.org/doi/10.1063/1.4772500

[79] Bir G. L., Aronov A. G. and Pikus G. E., *Soviet Physics JETP*, **42** (1976) 705 .

[80] Wu M., Jiang J. and Weng M., *Physics Reports*, **493** (2010) 61 .
URL http://www.sciencedirect.com/science/article/pii/S0370157310000955

[81] Fu H., Wang L.-W. and Zunger A., *Physical Review B*, **59** (1999) 5568.
URL https://link.aps.org/doi/10.1103/PhysRevB.59.5568

[82] Dyakonov M., *Spin Physics in Semiconductors* (Springer) 2008.

[83] Dresselhaus G., *Physical Review*, **100** (1955) 580.
URL https://link.aps.org/doi/10.1103/PhysRev.100.580

[84] Luttinger J. M., *Physical Review*, **102** (1956) 1030.
URL https://link.aps.org/doi/10.1103/PhysRev.102.1030

[85] Murakami S., Nagaosa N. and Zhang S.-C., *Science*, **301** (2003) 1348.
URL http://science.sciencemag.org/content/301/5638/1348

[86] Hilton D. J. and Tang C. L., *Physical Review Letters*, **89** (2002) 146601.
URL https://link.aps.org/doi/10.1103/PhysRevLett.89.146601

[87] Krishnamurthy S., van Schilfgaarde M. and Newman N., *Applied Physics Letters*, **83** (2003) 1761.
URL https://doi.org/10.1063/1.1606873

[88] Loren E. J., Rioux J., Lange C., Sipe J. E., van Driel H. M. and Smirl A. L., *Physical Review B*, **84** (2011) 214307.
URL https://journals.aps.org/prb/abstract/10.1103/PhysRevB.84.214307

[89] Meier L., Salis G., Shorubalko I., Gini E., Schön S. and Ensslin K., *Nature Physics*, **3** (2007) 650.

[90] Rojas-Sánchez J.-C., Cubukcu M., Jain A., Vergnaud C., Portemont C., Ducruet C., Barski A., Marty A., Vila L., Attané J.-P., Augendre E., Desfonds G., Gambarelli S., Jaffrès H., George J.-M. and Jamet M., *Physical Review B*, **88** (2013) 064403.
URL https://link.aps.org/doi/10.1103/PhysRevB.88.064403

[91] Ando K., Morikawa M., Trypiniotis T., Fujikawa Y., Barnes C. H. W. and Saitoh E., *Journal of Applied Physics*, **107** (2010) 113902.
URL http://scitation.aip.org/content/aip/journal/jap/107/11/10.1063/1.3418441

[92] Ando K., Morikawa M., Trypiniotis T., Fujikawa Y., Barnes C. H. W. and Saitoh E., *Applied Physics Letters*, **96** (2010) 082502.
URL http://scitation.aip.org/content/aip/journal/apl/96/8/10.1063/1.3327809

[93] Bottegoni F., Ferrari A., Isella G., Finazzi M. and Ciccacci F., *Physical Review B*, **88** (2013) 121201.
URL https://link.aps.org/doi/10.1103/PhysRevB.88.121201

[94] Lord Rayleigh F. R. S., *The London, Edinburgh, and Dublin Philosophical Magazine and Journal of Science*, **8** (1879) 261.
URL https://doi.org/10.1080/14786447908639684

[95] Bottegoni F., Celebrano M., Bollani M., Biagioni P., Isella G., Ciccacci F. and Finazzi M., *Nature Materials*, **13** (2014) 790.
URL http://www.nature.com/doifinder/10.1038/nmat4015%5Cnhttp://www.ncbi.nlm.nih.gov/pubmed/2495275

[96] McMaster W. H., *Reviews of Modern Physics*, **33** (1961) 8.
URL https://link.aps.org/doi/10.1103/RevModPhys.33.8

[97] Isella G., Bottegoni F., Ferrari A., Finazzi M. and Ciccacci F., *Applied Physics Letters*, **106** (2015) 232402.
URL https://doi.org/10.1063/1.4922290

[98] Žutić I., Fabian J. and Das Sarma S., *Physical Review B*, **64** (2001) 121201.
URL https://link.aps.org/doi/10.1103/PhysRevB.64.121201

[99] Hall R. N., *Physical Review*, **87** (1952) 387.
URL https://link.aps.org/doi/10.1103/PhysRev.87.387

[100] Bottegoni F., Zucchetti C., Isella G., Pinotti E., Finazzi M. and Ciccacci F., *Journal of Applied Physics*, **124** (2018) 033902.
URL https://doi.org/10.1063/1.5037653

[101] Spicer W. E., *Physical Review*, **112** (1958) 114.
URL https://link.aps.org/doi/10.1103/PhysRev.112.114

[102] Spicer W. E., *Applied Physics*, **12** (1977) 115.
URL https://doi.org/10.1007/BF00896137

[103] Pierce D. T., Celotta R. J., Wang G., Unertl W. N., Galejs A., Kuyatt C. E. and Mielczarek S. R., *Review of Scientific Instruments*, **51** (1980) 478.
URL https://doi.org/10.1063/1.1136250

[104] Bottegoni F., Ferrari A., Rortais F., Vergnaud C., Marty A., Isella G., Finazzi M., Jamet M. and Ciccacci F., *Physical Review B*, **92** (2015) 214403.
URL https://link.aps.org/doi/10.1103/PhysRevB.92.214403

[105] Sze S. M. and Ng K. K., *Physics of Semiconductor Devices* (John Wiley & sons) 2007.

[106] Zucchetti C., Isella G., Ciccacci F., Finazzi M. and Bottegoni F., *Proc. SPIE 11090, Spintronics XII*, (2019) 1109033.
URL https://www.spiedigitallibrary.org/conference-proceedings-of-spie/11090/2528167/Spin-transport

[107] Hilsum C., *Electronics Letters*, **10** (1974) 259.

[108] Li S. S. and Lindholm F. A., *Proceedings of the IEEE*, **56** (1968) 1256.

[109] Philipp H. R. and Taft E. A., *Physical Review*, **113** (1959) 1002.
URL https://link.aps.org/doi/10.1103/PhysRev.113.1002

[110] Boone C. T., Nembach H. T., Shaw J. M. and Silva T. J., *Journal of Applied Physics*, **113** (2013) 153906.
URL https://doi.org/10.1063/1.4801799

[111] Zhang W., Vlaminck V., Pearson J. E., Divan R., Bader S. D. and Hoffmann A., *Applied Physics Letters*, **103** (2013) 242414.
URL https://doi.org/10.1063/1.4848102

[112] Morota M., Niimi Y., Ohnishi K., Wei D. H., Tanaka T., Kontani H., Kimura T. and Otani Y., *Physical Review B*, **83** (2011) 174405.
URL https://link.aps.org/doi/10.1103/PhysRevB.83.174405

[113] Kurt H., Loloee R., Eid K., Pratt W. P. and Bass J., *Applied Physics Letters*, **81** (2002) 4787.
URL https://doi.org/10.1063/1.1528737

[114] Roy K., *Physical Review B*, **96** (2017) 174432.
URL https://link.aps.org/doi/10.1103/PhysRevB.96.174432

[115] Matsuzaka S., Ohno Y. and Ohno H., *Physical Review B*, **80** (2009) 241305.
URL https://link.aps.org/doi/10.1103/PhysRevB.80.241305

[116] Bottegoni F., Zucchetti C., Dal Conte S., Frigerio J., Carpene E., Vergnaud C., Jamet M., Isella G., Ciccacci F., Cerullo G. and Finazzi M., *Physical Review Letters*, **118** (2017) 167402.
URL https://link.aps.org/doi/10.1103/PhysRevLett.118.167402

[117] Stamm C., Murer C., Berritta M., Feng J., Gabureac M., Oppeneer P. M. and Gambardella P., *Physical Review Letters*, **119** (2017) 087203.
URL https://link.aps.org/doi/10.1103/PhysRevLett.119.087203

[118] Zucchetti C., Dau M.-T., Bottegoni F., Vergnaud C., Guillet T., Marty A., Beigné C., Gambarelli S., Picone A., Calloni A., Bussetti G., Brambilla A., Duò L., Ciccacci F., Das P. K., Fujii J., Vobornik I., Finazzi M. and Jamet M., *Physical Review B*, **98** (2018) 184418.
URL https://link.aps.org/doi/10.1103/PhysRevB.98.184418

[119] Yang Z. J. and Scheinfein M. R., *Journal of Applied Physics*, **74** (1993) 6810.
URL https://doi.org/10.1063/1.355081

[120] You C.-Y. and Shin S.-C., *Journal of Applied Physics*, **84** (1998) 541.
URL https://doi.org/10.1063/1.368058

[121] Tse W.-K., Fabian J., Žutić I. and Das Sarma S., *Physical Review B*, **72** (2005) 241303.
URL https://link.aps.org/doi/10.1103/PhysRevB.72.241303

[122] Pezzoli F., Bottegoni F., Trivedi D., Ciccacci F., Giorgioni A., Li P., Cecchi S., Grilli E., Song Y., Guzzi M., Dery H. and Isella G., *Physical Review Letters*, **108** (2012) 156603.
URL https://link.aps.org/doi/10.1103/PhysRevLett.108.156603

[123] Nastos F., Rioux J., Strimas-Mackey M., Mendoza B. S. and Sipe J. E., *Physical Review B*, **76** (2007) 205113.
URL https://link.aps.org/doi/10.1103/PhysRevB.76.205113

[124] Sturge M. D., *Physical Review*, **127** (1962) 768.
URL https://link.aps.org/doi/10.1103/PhysRev.127.768

[125] Tran M., Jaffrès H., Deranlot C., George J.-M., Fert A., Miard A. and Lemaître A., *Physical Review Letters*, **102** (2009) 036601.
URL https://link.aps.org/doi/10.1103/PhysRevLett.102.036601

[126] Li P. and Dery H., *Physical Review Letters*, **107** (2011) 107203.
URL https://link.aps.org/doi/10.1103/PhysRevLett.107.107203

[127] Song Y. and Dery H., *Physical Review B*, **86** (2012) 085201.
URL https://link.aps.org/doi/10.1103/PhysRevB.86.085201

[128] Oyarzï¿½n S., Rortais F., Rojas-Sï¿½nchez J.-C., Bottegoni F., Laczkowski P., Vergnaud C., Pouget S., Okuno H., Vila L., Attanï¿½ J.-P., Beignï¿½ C., Marty A., Gambarelli S., Ducruet C., Widiez J., George J.-M., Jaffrï¿½s H. and Jamet M., *Journal of the Physical Society of Japan*, **86** (2017) 011002.
URL https://doi.org/10.7566/JPSJ.86.011002

[129] Bottegoni F., Ferrari A., Cecchi S., Finazzi M., Ciccacci F. and Isella G., *Applied Physics Letters*, **102** (2013) 152411.
URL https://doi.org/10.1063/1.4802268

[130] Fan Y., Upadhyaya P., Kou X., Lang M., Takei S., Wang Z., Tang J., He L., Chang L.-T., Montazeri M., Yu G., Jiang W., Nie T., Schwartz R. N., Tserkovnyak Y. and Wang K. L., *Nature Materials*, **13** (2014) 699.

[131] Mellnik A. R., Lee J. S., Richardella A., Grab J. L., Mintun P. J., Fischer M. H., Vaezi A., Manchon A., Kim E.-A., Samarth N. and Ralph D. C., *Nature*, **511** (2014) 449.

[132] Wang Y., Deorani P., Banerjee K., Koirala N., Brahlek M., Oh S. and Yang H., *Physical Review Letters*, **114** (2015) 257202.
URL https://link.aps.org/doi/10.1103/PhysRevLett.114.257202

[133] DC M., Grassi R., Chen J.-Y., Jamali M., Hickey D. R., Zhang D., Zhao Z., Li H., Quarterman P., Lv Y., Li M., Manchon A., Mkhoyan K. A., Low T. and Wang J.-P., *Nature Materials*, **17** (2018) 800.

[134] Khang N. H. D., Ueda Y. and Hai P. N., *Nature Materials*, **17** (2018) 808.

[135] Ando K., Takahashi S., Harii K., Sasage K., Ieda J., Maekawa S. and Saitoh E., *Physical Review Letters*, **101** (2008) 036601.
URL https://link.aps.org/doi/10.1103/PhysRevLett.101.036601

[136] Azevedo A., Vilela-Leão L. H., Rodríguez-Suárez R. L., Lacerda Santos A. F. and Rezende S. M., *Physical Review B*, **83** (2011) 144402.
URL https://link.aps.org/doi/10.1103/PhysRevB.83.144402

[137] Obstbaum M., Härtinger M., Bauer H. G., Meier T., Swientek F., Back C. H. and Woltersdorf G., *Physical Review B*, **89** (2014) 060407.
URL https://link.aps.org/doi/10.1103/PhysRevB.89.060407

[138] Isasa M., Villamor E., Hueso L. E., Gradhand M. and Casanova F., *Physical Review B*, **91** (2015) 024402.
URL https://link.aps.org/doi/10.1103/PhysRevB.91.024402

[139] Finazzi M., Bottegoni F., Zucchetti C., Isella G. and Ciccacci F., *Scientific Reports*, **8** (2018) 17108.
URL https://www.nature.com/articles/s41598-018-35336-0

[140] Schottky W., *Zeitschrift für Physik*, **31** (1930) 913.

[141] Wallmark J. T., *Proceedings of the IRE*, **45** (1957) 474.

[142] Yu C. and Wang H., *Sensors*, **10** (2010) 10155.

[143] Spiesser A., Saito H., Fujita Y., Yamada S., Hamaya K., Yuasa S. and Jansen R., *Physical Review Applied*, **8** (2017) 064023.
URL https://link.aps.org/doi/10.1103/PhysRevApplied.8.064023

[144] Smirl A. L., Moss S. C. and Lindle J. R., *Physical Review B*, **25** (1982) 2645.
URL https://link.aps.org/doi/10.1103/PhysRevB.25.2645

[145] Zucchetti C., Bollani M., Isella G., Zani M., Finazzi M. and Bottegoni F., *APL Materials*, **7** (2019) 101122.
URL http://aip.scitation.org/doi/10.1063/1.5120967

[146] Reboud V., Gassenq A., Guilloy K., Osvaldo Dias G., Escalante J. M., Tardif S., Pauc N., Hartmann J. M., Widiez, J. Gomez E., Bellet Amalric E., Fowler D., Rouchon D., Duchemin I., Niquet Y. M., Rieutord F., Faist J., Geiger R., Zabel T., Marin E., Sigg H., Chelnokov A. and Calvo V., *Proceeding of SPIE*, **9752** (2016) 97520F.
URL https://doi.org/10.1117/12.2212597

[147] Jain S. and Roulston D., *Solid-State Electronics*, **34** (1991) 453 .
URL http://www.sciencedirect.com/science/article/pii/003811019190149S

[148] Khamari S. K., Dixit V. K. and Oak S. M., *Journal of Physics D: Applied Physics*, **44** (2011) 265104.
URL http://stacks.iop.org/0022-3727/44/i=26/a=265104

[149] Koike M., Shikoh E., Ando Y., Shinjo T., Yamada S., Hamaya K. and Shiraishi M., *Applied Physics Express*, **6** (2013) 023001.
URL http://stacks.iop.org/1882-0786/6/i=2/a=023001

[150] Engel H.-A., Halperin B. I. and Rashba E. I., *Physical Review Letters*, **95** (2005) 166605.
URL http://link.aps.org/doi/10.1103/PhysRevLett.95.166605

[151] Ando K. and Saitoh E., *Nature Communications*, **3** (2012) 629.

[152] Okamoto N., Kurebayashi H., Trypiniotis T., Farrer I., Ritchie D. A., Saitoh E., Sinova J., Mašek J., Jungwirth T. and Barnes C. H. W., *Nature Materials*, **13** (2014) 932.

[153] Rortais F., Oyarzï¿½n S., Bottegoni F., Rojas-Sï¿½nchez J.-C., Laczkowski P., Ferrari A., Vergnaud C., Ducruet C., Beignï¿½ C., Reyren N., Marty A., Attanï¿½ J.-P., Vila L., Gambarelli S., Widiez J., Ciccacci F., Jaffrï¿½s H., George J.-M. and Jamet M., *Journal of Physics: Condensed Matter*, **28** (2016) 165801.
URL http://stacks.iop.org/0953-8984/28/i=16/a=165801

[154] Varshni Y., *Physica*, **34** (1967) 149 .
URL http://www.sciencedirect.com/science/article/pii/0031891467900626

[155] Mitchell D. L. and Wallis R. F., *Physical Review*, **131** (1963) 1965.
URL https://link.aps.org/doi/10.1103/PhysRev.131.1965

[156] Debye P. P. and Conwell E. M., *Physical Review*, **93** (1954) 693.
URL https://link.aps.org/doi/10.1103/PhysRev.93.693

[157] Macfarlane G. G., McLean T. P., Quarrington J. E. and Roberts V., *Physical Review*, **108** (1957) 1377.
URL https://link.aps.org/doi/10.1103/PhysRev.108.1377

[158] Bottegoni F., Calloni A., Bussetti G., Camera A., Zucchetti C., Finazzi M., Duï¿½ L. and Ciccacci F., *Journal of Physics: Condensed Matter*, **28** (2016) 195001.
URL http://stacks.iop.org/0953-8984/28/i=19/a=195001

[159] Hatta S., Aruga T., Ohtsubo Y. and Okuyama H., *Physical Review B*, **80** (2009) 113309.
URL https://link.aps.org/doi/10.1103/PhysRevB.80.113309

[160] Zucchetti C., Bottegoni F., Calloni A., Bussetti G., Duï¿½ L., Finazzi M. and Ciccacci F., *Journal of Physics: Conference Series*, **903** (2017) 012024.
URL http://stacks.iop.org/1742-6596/903/i=1/a=012024

[161] Agergaard S., Sï¿½ndergaard C., Li H., Nielsen M. B., Hoffmann S. V., Li Z. and Hofmann P., *New Journal of Physics*, **3** (2001) 15.
URL http://stacks.iop.org/1367-2630/3/i=1/a=315

[162] Hirahara T., Nagao T., Matsuda I., Bihlmayer G., Chulkov E. V., Koroteev Y. M., Echenique P. M., Saito M. and Hasegawa S., *Physical Review Letters*, **97** (2006) 146803.
URL https://link.aps.org/doi/10.1103/PhysRevLett.97.146803

[163] Bian G., Miller T. and Chiang T.-C., *Physical Review B*, **80** (2009) 245407.
URL https://link.aps.org/doi/10.1103/PhysRevB.80.245407

[164] Hatta S., Ohtsubo Y., Miyamoto S., Okuyama H. and Aruga T., *Applied Surface Science*, **256** (2009) 1252 .
URL http://www.sciencedirect.com/science/article/pii/S0169433209007028
[165] Bertacco R. and Ciccacci F., *Physical Review B*, **59** (1999) 4207.
URL https://link.aps.org/doi/10.1103/PhysRevB.59.4207
[166] Bigi C., Das P. K., Benedetti D., Salvador F., Krizmancic D., Sergo R., Martin A., Panaccione G., Rossi G., Fujii J. and Vobornik I., *Journal of Synchrotron Radiation*, **24** (2017) 750.
URL https://doi.org/10.1107/S1600577517006907
[167] Pascual J. I., Bihlmayer G., Koroteev Y. M., Rust H.-P., Ceballos G., Hansmann M., Horn K., Chulkov E. V., Blügel S., Echenique P. M. and Hofmann P., *Physical Review Letters*, **93** (2004) 196802.
URL https://link.aps.org/doi/10.1103/PhysRevLett.93.196802
[168] Duggal V. P. and Rup R., *Journal of Applied Physics*, **40** (1969) 492.
URL https://doi.org/10.1063/1.1657426
[169] Garcia N., Kao Y. H. and Strongin M., *Physical Review B*, **5** (1972) 2029.
URL https://link.aps.org/doi/10.1103/PhysRevB.5.2029
[170] Lin Y.-M., Cronin S. B., Ying J. Y., Dresselhaus M. S. and Heremans J. P., *Applied Physics Letters*, **76** (2000) 3944.
URL https://doi.org/10.1063/1.126829
[171] Hirahara T., *Journal of Electron Spectroscopy and Related Phenomena*, **201** (2015) 98 .
URL http://www.sciencedirect.com/science/article/pii/S0368204814001674
[172] Zhang Z., Sun X., Dresselhaus M. S., Ying J. Y. and Heremans J., *Physical Review B*, **61** (2000) 4850.
URL https://link.aps.org/doi/10.1103/PhysRevB.61.4850
[173] Zhang W., Jungfleisch M. B., Jiang W., Pearson J. E. and Hoffmann A., *Journal of Applied Physics*, **117** (2015) 17C727.
URL https://doi.org/10.1063/1.4915479
[174] Matsushima M., Ando Y., Dushenko S., Ohshima R., Kumamoto R., Shinjo T. and Shiraishi M., *Applied Physics Letters*, **110** (2017) 072404.
URL https://doi.org/10.1063/1.4976691
[175] Isasa M., Martínez-Velarte M. C., Villamor E., Magén C., Morellón L., De Teresa J. M., Ibarra M. R., Vignale G., Chulkov E. V., Krasovskii E. E., Hueso L. E. and Casanova F., *Physical Review B*, **93** (2016) 014420.
URL https://link.aps.org/doi/10.1103/PhysRevB.93.014420
[176] Koroteev Y. M., Bihlmayer G., Gayone J. E., Chulkov E. V., Blügel S., Echenique P. M. and Hofmann P., *Physical Review Letters*, **93** (2004) 046403.
URL https://link.aps.org/doi/10.1103/PhysRevLett.93.046403
[177] Shen K., Vignale G. and Raimondi R., *Physical Review Letters*, **112** (2014) 096601.
URL https://link.aps.org/doi/10.1103/PhysRevLett.112.096601